

1-1-2009

## Partial wave analysis of the reaction $\gamma p \rightarrow p \omega$ and the search for nucleon resonances

M. Williams

Angela Biselli

Fairfield University, [abiselli@fairfield.edu](mailto:abiselli@fairfield.edu)

CLAS Collaboration

Follow this and additional works at: <https://digitalcommons.fairfield.edu/physics-facultypubs>

Copyright American Physical Society Publisher final version available at <http://prc.aps.org/abstract/PRC/v80/i6/e065209>

Peer Reviewed

---

### Repository Citation

Williams, M.; Biselli, Angela; and CLAS Collaboration, "Partial wave analysis of the reaction  $\gamma p \rightarrow p \omega$  and the search for nucleon resonances" (2009). *Physics Faculty Publications*. 45.

<https://digitalcommons.fairfield.edu/physics-facultypubs/45>

### Published Citation

M. Williams, et al. [CLAS Collaboration], "Partial wave analysis of the reaction  $\gamma p \rightarrow p \omega$  and the search for nucleon resonances," *Physical Review C* 80.6 (2009) DOI: 10.1103/PhysRevC.80.065209

This item has been accepted for inclusion in DigitalCommons@Fairfield by an authorized administrator of DigitalCommons@Fairfield. It is brought to you by DigitalCommons@Fairfield with permission from the rights-holder(s) and is protected by copyright and/or related rights. You are free to use this item in any way that is permitted by the copyright and related rights legislation that applies to your use. For other uses, you need to obtain permission from the rights-holder(s) directly, unless additional rights are indicated by a Creative Commons license in the record and/or on the work itself. For more information, please contact [digitalcommons@fairfield.edu](mailto:digitalcommons@fairfield.edu).

**Partial wave analysis of the reaction  $\gamma p \rightarrow p\omega$  and the search for nucleon resonances**

M. Williams,<sup>1,\*</sup> D. Applegate,<sup>1,†</sup> M. Bellis,<sup>1,†</sup> C. A. Meyer,<sup>1</sup> K. P. Adhikari,<sup>27</sup> M. Anghinolfi,<sup>18</sup> H. Baghdasaryan,<sup>27,36</sup> J. Ball,<sup>7</sup> M. Battaglieri,<sup>18</sup> I. Bedlinskiy,<sup>21</sup> B. L. Berman,<sup>14</sup> A. S. Biselli,<sup>1,11</sup> W. J. Briscoe,<sup>14</sup> W. K. Brooks,<sup>33,35</sup> V. D. Burkert,<sup>33</sup> S. L. Careccia,<sup>27</sup> D. S. Carman,<sup>33</sup> P. L. Cole,<sup>16</sup> P. Collins,<sup>3</sup> V. Crede,<sup>13</sup> A. D'Angelo,<sup>19,30</sup> A. Daniel,<sup>26</sup> R. De Vita,<sup>18</sup> E. De Sanctis,<sup>17</sup> A. Deur,<sup>33</sup> B. Dey,<sup>1</sup> S. Dhamija,<sup>12</sup> R. Dickson,<sup>1</sup> C. Djalali,<sup>32</sup> G. E. Dodge,<sup>27</sup> D. Doughty,<sup>8,33</sup> M. Dugger,<sup>3</sup> R. Dupre,<sup>2</sup> A. El Alaoui,<sup>20,‡</sup> L. Elouadrhiri,<sup>33</sup> P. Eugenio,<sup>13</sup> G. Fedotov,<sup>31</sup> S. Fegan,<sup>15</sup> A. Fradi,<sup>20</sup> M. Y. Gabrielyan,<sup>12</sup> M. Garçon,<sup>7</sup> G. P. Gilfoyle,<sup>29</sup> K. L. Giovanetti,<sup>22</sup> F. X. Girod,<sup>7,§</sup> W. Gohn,<sup>9</sup> E. Golovatch,<sup>31</sup> R. W. Gothe,<sup>32</sup> K. A. Griffioen,<sup>37</sup> M. Guidal,<sup>20</sup> N. Guler,<sup>27</sup> L. Guo,<sup>33,||</sup> K. Hafidi,<sup>2</sup> H. Hakobyan,<sup>35,38</sup> C. Hanretty,<sup>13</sup> N. Hassall,<sup>15</sup> K. Hicks,<sup>26</sup> M. Holtrop,<sup>24</sup> Y. Ilieva,<sup>14,32</sup> D. G. Ireland,<sup>15</sup> B. S. Ishkhanov,<sup>31</sup> E. L. Isupov,<sup>31</sup> S. S. Jawalkar,<sup>37</sup> H. S. Jo,<sup>20</sup> J. R. Johnstone,<sup>15</sup> K. Joo,<sup>9</sup> D. Keller,<sup>26</sup> M. Khandaker,<sup>25</sup> P. Khetarpal,<sup>28</sup> W. Kim,<sup>23</sup> A. Klein,<sup>27,||</sup> F. J. Klein,<sup>6</sup> Z. Krahn,<sup>1,¶</sup> V. Kubarovskiy,<sup>28,33</sup> S. V. Kuleshov,<sup>21,35</sup> V. Kuznetsov,<sup>23</sup> K. Livingston,<sup>15</sup> H. Y. Lu,<sup>32</sup> M. Mayer,<sup>27</sup> J. McAndrew,<sup>10</sup> M. E. McCracken,<sup>1</sup> B. McKinnon,<sup>15</sup> M. Mirazita,<sup>17</sup> V. Mokeev,<sup>31,33</sup> B. Moreno,<sup>20</sup> K. Moriya,<sup>1</sup> B. Morrison,<sup>3</sup> E. Munevar,<sup>14</sup> P. Nadel-Turonski,<sup>6</sup> C. S. Nepali,<sup>27</sup> S. Nicolai,<sup>20</sup> G. Niculescu,<sup>22</sup> I. Niculescu,<sup>22</sup> M. R. Niroula,<sup>27</sup> R. A. Niyazov,<sup>28,33</sup> M. Osipenko,<sup>18</sup> A. I. Ostrovidov,<sup>13</sup> M. Paris,<sup>33,\*\*</sup> K. Park,<sup>23,32,§</sup> S. Park,<sup>13</sup> E. Pasyuk,<sup>3</sup> S. Anefalos Pereira,<sup>17</sup> Y. Perrin,<sup>20,‡</sup> S. Pisano,<sup>20</sup> O. Pogorelko,<sup>21</sup> S. Pozdniakov,<sup>21</sup> J. W. Price,<sup>4</sup> S. Procureur,<sup>7</sup> D. Protopopescu,<sup>15</sup> G. Ricco,<sup>18</sup> M. Ripani,<sup>18</sup> B. G. Ritchie,<sup>3</sup> G. Rosner,<sup>15</sup> P. Rossi,<sup>17</sup> F. Sabatié,<sup>7</sup> M. S. Saini,<sup>13</sup> J. Salamanca,<sup>16</sup> C. Salgado,<sup>25</sup> D. Schott,<sup>12</sup> R. A. Schumacher,<sup>1</sup> H. Seraydaryan,<sup>27</sup> Y. G. Sharabian,<sup>33</sup> E. S. Smith,<sup>33</sup> D. I. Sober,<sup>6</sup> D. Sokhan,<sup>10</sup> S. S. Stepanyan,<sup>23</sup> P. Stoler,<sup>28</sup> I. I. Strakovsky,<sup>14</sup> S. Strauch,<sup>14,32</sup> M. Taiuti,<sup>18</sup> D. J. Tedeschi,<sup>32</sup> S. Tkachenko,<sup>27</sup> M. Ungaro,<sup>9,28</sup> M. F. Vineyard,<sup>34</sup> E. Voutier,<sup>20,‡</sup> D. P. Watts,<sup>15,††</sup> D. P. Weygand,<sup>33</sup> M. H. Wood,<sup>5,32</sup> J. Zhang,<sup>27</sup> and B. Zhao<sup>9,††</sup>

(CLAS Collaboration)

<sup>1</sup>Carnegie Mellon University, Pittsburgh, Pennsylvania 15213, USA<sup>2</sup>Argonne National Laboratory, Argonne, Illinois 60441, USA<sup>3</sup>Arizona State University, Tempe, Arizona 85287-1504, USA<sup>4</sup>California State University, Dominguez Hills, Carson, California 90747, USA<sup>5</sup>Canisius College, Buffalo, New York 14208, USA<sup>6</sup>Catholic University of America, Washington, DC 20064, USA<sup>7</sup>CEA, Centre de Saclay, Irfu/Service de Physique Nucléaire, F-91191 Gif-sur-Yvette, France<sup>8</sup>Christopher Newport University, Newport News, Virginia 23606, USA<sup>9</sup>University of Connecticut, Storrs, Connecticut 06269, USA<sup>10</sup>Edinburgh University, Edinburgh EH9 3JZ, United Kingdom<sup>11</sup>Fairfield University, Fairfield Connecticut 06824, USA<sup>12</sup>Florida International University, Miami, Florida 33199, USA<sup>13</sup>Florida State University, Tallahassee, Florida 32306, USA<sup>14</sup>The George Washington University, Washington, DC 20052, USA<sup>15</sup>University of Glasgow, Glasgow G12 8QQ, United Kingdom<sup>16</sup>Idaho State University, Pocatello, Idaho 83209, USA<sup>17</sup>INFN, Laboratori Nazionali di Frascati, I-00044 Frascati, Italy<sup>18</sup>INFN, Sezione di Genova, I-16146 Genova, Italy<sup>19</sup>INFN, Sezione di Roma Tor Vergata, I-00133 Rome, Italy<sup>20</sup>Institut de Physique Nucléaire ORSAY, Orsay, France<sup>21</sup>Institute of Theoretical and Experimental Physics, Moscow RU-117259, Russia<sup>22</sup>James Madison University, Harrisonburg, Virginia 22807, USA<sup>23</sup>Kyungpook National University, Daegu 702-701, Republic of Korea<sup>24</sup>University of New Hampshire, Durham, New Hampshire 03824-3568, USA<sup>25</sup>Norfolk State University, Norfolk, Virginia 23504, USA<sup>26</sup>Ohio University, Athens, Ohio 45701, USA<sup>27</sup>Old Dominion University, Norfolk, Virginia 23529, USA<sup>28</sup>Rensselaer Polytechnic Institute, Troy, New York 12180-3590, USA<sup>29</sup>University of Richmond, Richmond, Virginia 23173, USA<sup>30</sup>Universita' di Roma Tor Vergata, I-00133 Rome, Italy<sup>31</sup>Skobel'syn Nuclear Physics Institute, Moscow RU-119899, Russia<sup>32</sup>University of South Carolina, Columbia, South Carolina 29208, USA<sup>33</sup>Thomas Jefferson National Accelerator Facility, Newport News, Virginia 23606, USA<sup>34</sup>Union College, Schenectady, New York 12308, USA<sup>35</sup>Universidad Técnica Federico Santa María, Casilla 110-V Valparaíso, Chile<sup>36</sup>University of Virginia, Charlottesville, Virginia 22901, USA<sup>37</sup>College of William and Mary, Williamsburg, Virginia 23187-8795, USA

<sup>38</sup>*Yerevan Physics Institute, 375036 Yerevan, Armenia*  
(Received 23 August 2009; published 30 December 2009)

An event-based partial wave analysis (PWA) of the reaction  $\gamma p \rightarrow p\omega$  has been performed on a high-statistics dataset obtained using the CLAS at Jefferson Lab for center-of-mass energies from threshold up to 2.4 GeV. This analysis benefits from access to the world's first high-precision spin-density matrix element measurements, available to the event-based PWA through the decay distribution of  $\omega \rightarrow \pi^+\pi^-\pi^0$ . The data confirm the dominance of the  $t$ -channel  $\pi^0$  exchange amplitude in the forward direction. The dominant resonance contributions are consistent with the previously identified states  $F_{15}(1680)$  and  $D_{13}(1700)$  near threshold, as well as the  $G_{17}(2190)$  at higher energies. Suggestive evidence for the presence of a  $J^P = 5/2^+$  state around 2 GeV, a “missing” state, has also been found. Evidence for other states is inconclusive.

DOI: [10.1103/PhysRevC.80.065209](https://doi.org/10.1103/PhysRevC.80.065209)

PACS number(s): 11.80.Cr, 11.80.Et, 13.30.Eg, 14.20.Gk

## I. INTRODUCTION

Studying near-threshold  $\omega$  photoproduction presents an interesting opportunity to search for new baryon resonances. Measurements made by previous experiments have produced relatively high-precision cross sections at most production angles; however, precise spin-density matrix elements have only been measured at very forward angles and at higher energies [1–5]. In the near-threshold region, the only previously published spin-density matrix results, which come from the SAPHIR Collaboration, constitute a total of eight data points in the energy range from  $\omega$  photoproduction threshold up to a center-of-mass energy,  $W$ , of about 2.4 GeV [5].

A number of theoretical studies have been undertaken with the goal of extracting resonance contributions to  $\omega$  photoproduction from these data. All of the authors agree on the importance of contributions from  $\pi^0$  exchange in the  $t$  channel; however, discrepancies exist on the importance of various resonance contributions. In the calculations of Oh *et al.* [6], the dominant resonance contributions are found to be from a “missing”  $P_{13}(1910)$  state (i.e., a state predicted by the constituent quark model but not observed experimentally) and from a  $D_{13}(1960)$  state. In contrast to this, Titov and Lee [7] find the most significant resonance contributions to be from the  $D_{13}(1520)$  and  $F_{15}(1680)$  states. The quark model calculations made by Zhao [8] find that the two most important resonance contributions to  $\omega$  photoproduction come from the

$P_{13}(1720)$  and  $F_{15}(1680)$  states. The  $P_{11}(1710)$  and  $P_{13}(1900)$  states were found to be the dominant resonance contributions in the coupled-channel analysis of Penner and Mosel [9].

All of the models mentioned above were fit solely to differential cross sections. A more recent analysis [10] also included the spin-density matrix elements published by the SAPHIR Collaboration [5]. This work found the largest resonant contributions to  $\omega$  photoproduction to be from the subthreshold  $D_{15}(1675)$  and  $F_{15}(1680)$  states. The authors noted the importance of the strong additional constraints placed on their model by the polarization information and concluded that: *there is urgent need for precise measurements of the spin-density matrix in more narrow energy bins to pin down the reaction picture.*

Recently published results from the CEBAF Large Acceptance Spectrometer (CLAS) have provided such measurements [11]. In the center-of-mass (c.m.) energy range from threshold up to 2.84 GeV, differential cross section results were reported at 1960 points in  $W$  and  $\cos\theta_{\text{c.m.}}^\omega$ . The experiment did not use a polarized beam or a polarized target; thus, only the  $\rho_{00}^0$ ,  $\rho_{1-1}^0$ , and  $\text{Re}(\rho_{10}^0)$  elements of the spin-density matrix could be determined (the definitions of which can be found in [12]). These results were reported at 2015 points in  $W$  and  $\cos\theta_{\text{c.m.}}^\omega$ . The increase in precision for  $\rho_{MM}^0$ , in the energy range overlapping the SAPHIR results, is approximately a factor of 148.

In this paper, we present an *event-based mass-independent* partial wave analysis (PWA) of these data, i.e., the data are only divided into narrow c.m. energy bins. In each of these narrow bins, the spin-independent part of any resonance propagator—a complex function of  $W$ —is approximated as a constant complex number. This allows us to reduce model dependence in our treatment of resonances (see Sec. III C for further discussion on this topic).

The data used in our analysis were obtained using the CLAS housed in Hall B at the Thomas Jefferson National Accelerator Facility. Real photons were produced via bremsstrahlung from a 4.02 GeV electron beam. The momenta of the recoiling electrons were then analyzed in order to obtain the energy of the photons with an uncertainty of 0.1% [13]. The physics target was filled with liquid hydrogen. The  $\omega \rightarrow \pi^+\pi^-\pi^0$  decay was used to select the reaction of interest. The momenta of the charged particles ( $p$ ,  $\pi^+$ ,  $\pi^-$ ) were determined using the CLAS with an uncertainty of approximately 0.5%. The neutral

\*Current address: Imperial College London, London SW7 2AZ, United Kingdom.

†Current address: Stanford University, Stanford, CA 94305, USA.

‡Current address: LPSC-Grenoble, France.

§Current address: Thomas Jefferson National Accelerator Facility, Newport News, Virginia 23606, USA.

||Current address: Los Alamos National Laboratory, New Mexico, NM, USA.

\*Current address: University of Minnesota, Minneapolis, MN 55455, USA.

\*\*Current address: The George Washington University, Washington, DC 20052, USA.

††Current address: Edinburgh University, Edinburgh EH9 3JZ, United Kingdom.

‡‡Current address: College of William and Mary, Williamsburg, Virginia 23187-8795, USA.

$\pi^0$  was reconstructed using kinematic fitting. More details concerning the analysis techniques can be found in [11,14]. A detailed description of the CLAS can be found in [15].

In total, the dataset consists of over 10 million signal events divided into 112 10-MeV wide c.m. energy bins. Our primary interest is in extracting possible nucleon resonance contributions; thus, we have restricted our PWA to include only bins with  $W < 2.4$  GeV. In total, 67 c.m. energy bins were used in the PWA (the  $W = 1.955$  GeV bin was excluded due to issues with the normalization calculation [11]). This work represents the first event-based PWA results on baryons from photoproduction data.

## II. PWA FORMULAS

As stated above, to limit theoretical model dependence we divided our data into 10-MeV wide  $W$  bins. Thus, all formulas written below are intended to describe data from a narrow c.m. energy range. In all of the work that follows,  $p_i$ ,  $p_f$ ,  $q$ , and  $k$  will be used for the initial proton, final proton,  $\omega$ , and photon four-momenta. The  $z$ -axis in the overall c.m. frame, defined by  $\hat{k}$ , is used as the angular momentum quantization axis. The Mandelstam variables are defined as

$$s = (p_i + k)^2 = (p_f + q)^2, \quad (1a)$$

$$t = (q - k)^2 = (p_i - p_f)^2, \quad (1b)$$

$$u = (p_i - q)^2 = (p_f - k)^2. \quad (1c)$$

The mass of the proton and  $\omega$  are denoted as  $w_p$  and  $w_\omega$ , respectively.

The Lorentz invariant transition amplitude,  $\mathcal{M}$ , of the process  $\gamma p \rightarrow p\omega \rightarrow p\pi^+\pi^-\pi^0$ , can be written as

$$|\mathcal{M}(\vec{\alpha}, \vec{x})|^2 = \sum_{m_i, m_\gamma, m_f} \left| \sum_a \mathcal{A}_{m_i, m_\gamma, m_f}^a(\vec{\alpha}, \vec{x}) \right|^2, \quad (2)$$

where  $m_i$ ,  $m_\gamma$ ,  $m_f$  are the initial proton, incident photon, and final proton spin projections,  $\mathcal{A}_{m_i, m_\gamma, m_f}^a$  are the partial wave amplitudes (the form of which is discussed in Sec. III),  $\vec{x}$  denotes the complete set of kinematic variables describing the reaction and  $\vec{\alpha}$  are the unknown parameters to be determined by the fit. We denote the detector acceptance by  $\eta(\vec{x})$  and the phase-space volume as  $d\Phi(\vec{x}) = \phi(\vec{x})d\vec{x}$ . A more detailed description of the work presented in this section is given in [14].

### A. Likelihood

All of our fits are event-based; thus, the data were only binned in  $W$ . To obtain estimators for the unknown parameters,  $\hat{\alpha}$ , we employ the extended unbinned maximum likelihood method. The work detailed in this section is based on that of Chung [16]; however, the normalizations we have developed differ from his work. The likelihood function is defined as

$$\mathcal{L} = \left[ \frac{\bar{n}(\vec{\alpha})^n}{n!} e^{-\bar{n}(\vec{\alpha})} \right] \prod_i^n \mathcal{P}(\vec{\alpha}, \vec{x}_i), \quad (3)$$

where the term in brackets is the Poisson probability of obtaining  $n$  events given the expected number  $\bar{n}(\vec{\alpha})$  (the calculation of which is discussed below),  $\vec{x}_i$  represents the

complete set of kinematic variables of the  $i$ th event, and  $\mathcal{P}(\vec{\alpha}, \vec{x})$  is the probability density function given by

$$\mathcal{P}(\vec{\alpha}, \vec{x}_i) = \frac{|\mathcal{M}(\vec{\alpha}, \vec{x}_i)|^2 \eta(\vec{x}_i) \phi(\vec{x}_i)}{\int |\mathcal{M}(\vec{\alpha}, \vec{x})|^2 \eta(\vec{x}) \phi(\vec{x}) d\vec{x}}. \quad (4)$$

From left to right, Eq. (4) accounts for the relative strength of the transition amplitude, the detection probability, and the available phase space for the  $i$ th event. Calculation of the denominator, which normalizes the probability density function, is discussed below. The estimators  $\hat{\alpha}$  are then found by maximizing  $\mathcal{L}$ .

### B. Normalization

The expected number of signal events for a given set of parameters is given by

$$\bar{n}(\vec{\alpha}) = \frac{\mathcal{T}(s)(2\pi)^4}{8(s - w_p^2)} \int |\mathcal{M}(\vec{\alpha}, \vec{x})|^2 \eta(\vec{x}) d\Phi(\vec{x}), \quad (5)$$

which includes the average over initial spin states

$$\mathcal{T}(s) = \frac{\mathcal{F}(s) \rho_{\text{targ}} \ell_{\text{targ}} N_A b}{A_{\text{targ}}} \quad (6)$$

is the ‘‘target factor’’ obtained from the target density,  $\rho_{\text{targ}}$ , length,  $\ell_{\text{targ}}$ , and atomic number,  $A_{\text{targ}}$ ; along with Avogadro’s number,  $N_A$ ; the branching fraction of  $\omega \rightarrow \pi^+\pi^-\pi^0$ ,  $b$ ; and the integrated photon flux in each  $W$  bin,  $\mathcal{F}(s)$ .

The integral in Eq. (5) must be done numerically due to the lack of an analytic expression for the detector acceptance. Monte Carlo events were generated in each  $W$  bin according to  $\gamma p \rightarrow p\omega$  (the  $\omega$  mass was generated according to a Breit-Wigner distribution),  $\omega \rightarrow \pi^+\pi^-\pi^0$  phase space and then run through a GEANT-based detector simulation package (discussed in detail in [11,14]). This procedure simulates the acceptance of the detector by rejecting events that would not have survived the data analysis, i.e., for each generated event, the acceptance factor  $\eta(\vec{x}_i) = 0$  or 1. The integral can then be approximated by

$$\int |\mathcal{M}(\vec{\alpha}, \vec{x})|^2 \eta(\vec{x}) d\Phi(\vec{x}) \approx \frac{\int d\Phi(\vec{x})}{n_{\text{gen}}} \sum_i^{n_{\text{acc}}} |\mathcal{M}(\vec{\alpha}, \vec{x}_i)|^2, \quad (7)$$

where  $n_{\text{gen}}(n_{\text{acc}})$  is the number of generated (accepted) Monte Carlo events and

$$\int d\Phi(\vec{x}) = \frac{\{[s - (w_p + w_\omega)^2][s - (w_p - w_\omega)^2]\}^{1/2}}{4(2\pi)^5 s} \quad (8)$$

is the volume of the two-body  $p\omega$  phase space (the  $3\pi$  phase-space volume is factored into the normalization of the  $\omega$  decay amplitude).

Using Eqs. (7) and (8), Eq. (5) can be rewritten as

$$\begin{aligned} \bar{n}(\vec{\alpha}) &= \frac{\{[s - (w_p + w_\omega)^2][s - (w_p - w_\omega)^2]\}^{1/2}}{64\pi s(s - w_p^2)} \\ &\times \frac{\mathcal{T}(s)}{n_{\text{gen}}} \sum_i^{n_{\text{acc}}} |\mathcal{M}(\vec{\alpha}, \vec{x}_i)|^2. \end{aligned} \quad (9)$$

This normalization allows us to use physical coupling constants in our event-based fits, i.e., it allows us to put our

parameters on an absolute scale. Thus, our normalization scheme permits direct theoretical input.

### C. Log likelihood

Due to the monotonically increasing nature of the natural logarithm, the likelihood,  $\mathcal{L}$ , defined in Eq. (3) can be maximized by minimizing

$$-\ln \mathcal{L} = -n \ln \bar{n}(\vec{\alpha}) + \ln n! + \bar{n}(\vec{\alpha}) - \sum_i^n \ln \mathcal{P}(\vec{\alpha}, \vec{x}_i), \quad (10)$$

which, using Eqs. (4) and (5), can be rewritten as

$$\begin{aligned} -\ln \mathcal{L} &= \ln n! + \bar{n}(\vec{\alpha}) + n \ln \frac{8(s - w_p^2)}{T(s)(2\pi)^4} \\ &\quad - \sum_i^n \ln |\mathcal{M}(\vec{\alpha}, \vec{x}_i)|^2 \eta(\vec{x}_i) \phi(\vec{x}_i). \end{aligned} \quad (11)$$

Neglecting terms that do not depend on the parameters, we can then rewrite Eq. (11) as follows:

$$-\ln \mathcal{L} = - \sum_i^n \ln |\mathcal{M}(\vec{\alpha}, \vec{x}_i)|^2 + \bar{n}(\vec{\alpha}) + \text{const.} \quad (12)$$

We note here that for any set of estimators that minimize Eq. (12), the expected number of events is  $\bar{n}(\hat{\alpha}) = n$ .

### D. Handling background

To accurately extract partial wave contributions to  $\omega$  photoproduction, background events, i.e., non- $\omega$  events, must be separated from the signal in a way that preserves all kinematic correlations. The method we applied to our data, described in detail in [11,14,17], assigned each event a signal quality factor, or  $Q$  factor. This background was assumed to be noninterfering. Following our previous work [17], we can rewrite Eq. (12) using these  $Q$  factors as

$$-\ln \mathcal{L} = - \sum_i^n Q_i \ln |\mathcal{M}(\vec{\alpha}, \vec{x}_i)|^2 + \bar{n}(\vec{\alpha}) + \text{const.}, \quad (13)$$

where  $Q_i$  is the  $Q$  factor for the  $i$ th event. Thus, the  $Q$  factors are used to weight each event's contribution to the likelihood. We also note that in the literature, the  $t$ - and  $u$ -channel contributions are often referred to as *background*. This *theoretical* background is not to be confused with the experimental background discussed here. In this analysis, the theoretical backgrounds were allowed to interfere with the  $s$ -channel amplitudes in our PWA.

## III. PWA AMPLITUDES

The choice of which amplitudes to include to describe the data is partially motivated by experimental measurements. The  $\omega$  photoproduction cross section is known to have a strong forward peak, even at near-threshold energies [11]. At higher energies, the cross section develops a rather pronounced backward peak as well [11]. These features are typically

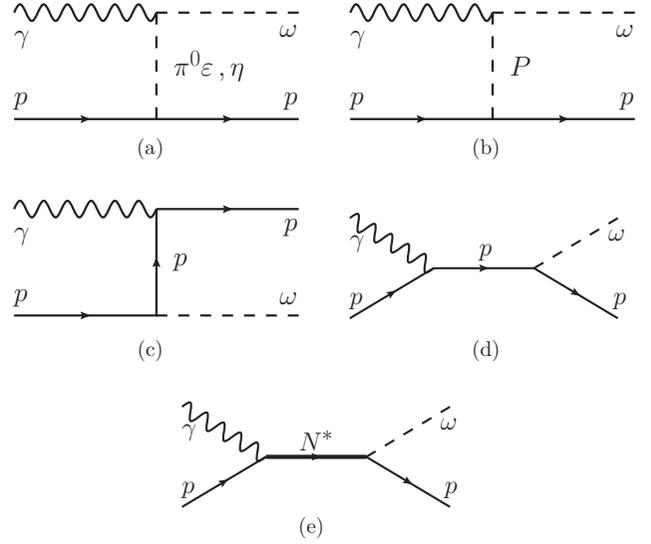


FIG. 1. Feynman diagrams for the amplitudes used in our analysis. The images were produced using the JaxoDraw package [19].

associated with meson and nucleon exchanges in the  $t$  and  $u$  channels, respectively. The recent CLAS data also possess a number of features in the cross sections and spin-density matrix elements suggestive of resonance contributions [11]. Thus, it would seem that  $s$ -,  $t$ -, and  $u$ -channel amplitudes may be required to fully describe the data (see Fig. 1). The formalism used to construct these amplitudes is described in detail elsewhere [14], below we simply give an overview of the different types of amplitudes used in our analysis. All of these amplitudes were computed using the qft++ package [18], which performs numerical computations of quantum field theory expressions.

### A. $\omega \rightarrow \pi^+ \pi^- \pi^0$

The  $\omega \rightarrow \pi^+ \pi^- \pi^0$  amplitude can be written in terms of the isovectors,  $\vec{I}_\pi$ , and the four-momenta,  $p_\pi$ , of the pions, along with the  $\omega$  four-momentum ( $q$ ), polarization ( $\epsilon$ ), and spin projection,  $m_\omega$ , as

$$\begin{aligned} \mathcal{A}_{\omega \rightarrow \pi^+ \pi^- \pi^0}^{m_\omega} &\propto [(\vec{I}_{\pi^+} \times \vec{I}_{\pi^0}) \cdot \vec{I}_{\pi^-}] \\ &\quad \times \epsilon_{\mu\nu\alpha\beta} p_{\pi^+}^\nu p_{\pi^-}^\alpha p_{\pi^0}^\beta \epsilon^\mu(q, m_\omega), \end{aligned} \quad (14)$$

which is fully symmetric under interchange of the three pions. For this reaction, where all final states contain  $\omega \rightarrow \pi^+ \pi^- \pi^0$ , the isovector triple product simply contributes a factor to the global phase of all amplitudes. In the  $\omega$  rest frame, Eq. (14) simplifies to

$$\mathcal{A}_{\omega \rightarrow \pi^+ \pi^- \pi^0}^{m_\omega} \propto (\vec{p}_{\pi^+} \times \vec{p}_{\pi^-}) \cdot \vec{\epsilon}(m_\omega), \quad (15)$$

which is the standard nonrelativistic result [20].

### B. $t$ and $u$ channels

Previous studies of forward  $\omega$  photoproduction data have shown that the reaction is dominated at low energies by pion exchange and at higher energies by diffractive processes, i.e.,

Pomeron exchange (see, e.g., [1]). We have chosen to use the nonresonant terms included in the model of Oh, Titov, and Lee (OTL) [6] in our partial wave analysis. The OTL Pomeron exchange amplitude follows the work of Donnachie and Landshoff [21] with the unknown parameters fixed by fitting to high energy vector meson cross section data.

The OTL model also includes pseudoscalar meson exchange amplitudes obtained from the following Lagrangians:

$$\mathcal{L}_{\phi pp} = -i g_{\phi pp} \bar{\psi} \gamma^5 \psi \phi, \quad (16a)$$

$$\mathcal{L}_{\gamma\phi\omega} = e \frac{g_{\gamma\phi\omega}}{w_\omega} \epsilon^{\mu\nu\alpha\beta} \partial_\mu \omega_\nu \partial_\alpha A_\beta \phi, \quad (16b)$$

where  $\phi = (\pi, \eta)$ ,  $A_\mu$ , and  $\psi$  denote the pseudoscalar, photon, and proton fields, respectively. The vertices in these amplitudes were dressed using form factors of the type

$$F(t, \Lambda) = \frac{\Lambda^2 - w_\phi^2}{\Lambda^2 - t}, \quad (17)$$

where  $\Lambda$  is the cutoff parameter for the interaction and  $w_\phi$  is the mass of the exchanged particle. The larger mass and weaker coupling constants of the  $\eta$  suppress its contribution relative to that of the pion.

Nucleon pole terms were obtained from the Lagrangians

$$\mathcal{L}_{\gamma pp} = -e \bar{\psi} \left( \gamma^\mu - \frac{\kappa_p}{2m_p} \sigma^{\mu\nu} \partial_\nu \right) A_\mu \psi, \quad (18a)$$

$$\mathcal{L}_{\omega pp} = -g_{\omega pp} \bar{\psi} \left( \gamma^\mu - \frac{\kappa_\omega}{2m_p} \sigma^{\mu\nu} \partial_\nu \right) \omega_\mu \psi. \quad (18b)$$

The form factor

$$F_N(x) = \frac{\Lambda_N^4}{\Lambda_N^4 - (x - w_p^2)^2}, \quad (19)$$

where  $x = (s, u)$ , was included to dress the corresponding vertices. The amplitudes were also modified to preserve gauge invariance. The details concerning these modifications, along with the values of the parameters used in the model can be found in [6].

In the near-threshold region, the high precision spin-density matrix results published by CLAS confirm the dominance of  $t$ -channel  $\pi^0$  exchange in the forward direction; however, at higher energies the existing theoretical models fail to reproduce the CLAS data [22]. The Pomeron amplitudes are able to describe the energy dependence of the forward cross section, but fail to adequately describe the spin-density matrix elements. The unknown parameters present in the nucleon exchange amplitudes can be modified to describe the backward-angle data at higher energies if some assumptions, the reliability of which are unknown, are made [22].

Our analysis is restricted to the energy range from threshold up to 2.4 GeV. For c.m. energies below 2 GeV, the  $\pi^0$  exchange amplitude dominates the  $t$ -channel contributions. In the higher energy range used in our analysis, the  $\pi^0$  contribution is still substantially larger than that of the Pomeron. Thus, the deficiencies in the Pomeron amplitudes (discussed above) should not greatly affect our PWA results. For this reason, we have chosen to use the OTL  $t$ -channel terms with the parameter values obtained in that analysis [6]. Due to the unreliability of the assumptions under which the nucleon

exchange parameters were determined, we have decided not to include these amplitudes in our analysis, i.e., we do not include any  $u$ -channel terms in our fits. The effect of this choice on our conclusions was found to be negligible (see Sec. V).

### C. Resonant waves

The formalism used to construct our resonant amplitudes is described fully in [14]. It involves the use of relativistic tensor operators and is similar to the framework employed by Anisovich *et al.* [23].

As discussed above, we do not impose resonant-like shapes on our  $s$ -channel waves. Instead, we divide our data into narrow c.m. energy bins. In each of these bins, the mass-dependence of an  $s$ -channel wave with spin  $J$  and parity  $P$ , which we will denote  $\mathcal{R}_{J^P}(s)$ , is approximated by a constant complex number:

$$\mathcal{R}_{J^P}(s) \approx \sum_b r_{J^P}^b e^{i\phi_{J^P}^b} \Theta(\delta - |\sqrt{s} - W_b|), \quad (20)$$

where the sum is over the 10-MeV wide c.m. energy bins,  $r_{J^P}^b$ ,  $\phi_{J^P}^b$  are the strength and phase of the mass dependence in each bin, respectively, and  $\delta \equiv 5$  MeV is the maximum distance in any bin from the centroid  $W_b$ . The resonant waves then enter into our fits according to

$$A_{m_i, m_\gamma, m_f}^{J^P, LS_i, LS_f} = g_{LS_i}^{J^P} g_{LS_f}^{J^P} \mathcal{R}_{J^P}(s) A_{m_i, m_\gamma, m_f}^{J^P, LS_i, LS_f}, \quad (21)$$

where  $LS_{i(f)}$  are the angular momentum quantum numbers of the initial (final) state,  $g_{LS_{i(f)}}^{J^P}$  are the unknown coupling constants to these states, and  $A$  is the covariant amplitude obtained using the formalism described in [14].

The values extracted for each  $s$ -channel wave's  $r_{J^P}^b$  and  $\phi_{J^P}^b$  parameters can be used to search for evidence of nucleon resonance contributions in that wave. For every fit iteration run in each  $W$  bin (multiple iterations are run to alleviate problems caused by local minima), these parameters are started at random values that include the entire physically allowed range of the parameter. For example,  $\phi_{J^P}^b$  is started randomly in the range  $[0, 2\pi)$ . Estimators for the parameters are then found by maximizing the likelihoods independently in each  $W$  bin. In this way, the mass dependence of the waves is extracted unbiasedly. If resonant-like features are found in the cross sections and phase motion of the  $s$ -channel waves, then this is very strong evidence that resonances do contribute to the scattering amplitude.

If the strength observed in an  $s$ -channel wave is due to a single resonant state, then  $\mathcal{R}_{J^P}(s)$  should be (at least qualitatively) described by a constant-width Breit-Wigner line shape of the form:

$$\text{BW}(s) = \frac{w\Gamma}{s - w^2 + iw\Gamma}, \quad (22)$$

where  $w$  and  $\Gamma$  denote the mass and width of the state, respectively. If, however, the strength in the wave is caused by multiple resonant states or from a nonresonant process, then the use of a Breit-Wigner line shape is not valid. The line shape given in Eq. (22) neglects the kinematics and dynamics

of the mass dependence of the resonance. This can be an issue, e.g., near threshold. This will be addressed below.

#### IV. RESULTS

Before examining our results, it is important to reiterate the goals of our analysis. We are attempting to extract strong resonance contributions to  $\omega$  photoproduction in a least model-dependent way. We do not enforce resonance shapes on the mass dependence of our partial waves. Instead, we first extract the strengths and phase motion of our partial waves independently in each  $W$  bin. This stage will be referred to as a partial wave extraction (PWE). The second stage involves comparing the results of the PWE to what is expected from resonances in a mass-dependent fit (MDF). The PWE's are performed using unbinned extended maximum likelihood fits to the data in each  $W$  bin. The MDF's are simply  $\chi^2$  fits to the phase differences obtained between partial waves in a given  $W$  region.

We are not looking to build a complete model of  $\omega$  photoproduction, i.e., we do not claim that the fits discussed below contain all of the amplitudes that contribute to this reaction. Because of this, we do not expect the physical observables extracted from our fits to provide perfect descriptions of our measurements; however, the descriptions in many kinematic regions are very good. Finally, we are not attempting to extract all resonance contributions to  $\omega$  photoproduction, only the most significant.

##### A. Choice of wave sets

It is important to have a systematic method for selecting wave sets. As discussed in Sec. III B, all of the wave sets used in our analysis contain the OTL  $t$ -channel terms (which contain no free parameters) and no  $u$ -channel terms. Systematic studies show that the effects on extracted resonance parameters due to the choice of the nonresonant model are small (see Sec. V).

The mass-independent nature of our procedure, i.e., the bin-to-bin freedom of the resonance parameters, makes the use of smaller wave sets advantageous. For this reason, we began our wave selection process by scanning the entire energy range of interest,  $1.72 \text{ GeV} < W < 2.4 \text{ GeV}$ , using the OTL  $t$ -channel terms along with waves from a single spin-parity,  $J^P$ . The goal of this scan was to identify (possible) energy ranges where waves of a given  $J^P$  perform significantly better than waves of any other spin-parity. This information alone does not constitute evidence of resonance production; however, it can serve as a guide as to which waves are more likely to contribute strongly to  $\omega$  photoproduction.

Given a pair of fits run with different wave sets, the difference in the log likelihoods obtained from the fits,  $\Delta \ln \mathcal{L} \equiv \ln \mathcal{L}_a - \ln \mathcal{L}_b$ , can be used to quantitatively determine which fit best describes the data. If  $\Delta \ln \mathcal{L} > 0$ , then wave set  $a$  provides a better description of the data than wave set  $b$ , while  $\Delta \ln \mathcal{L} < 0$  implies the converse is true.

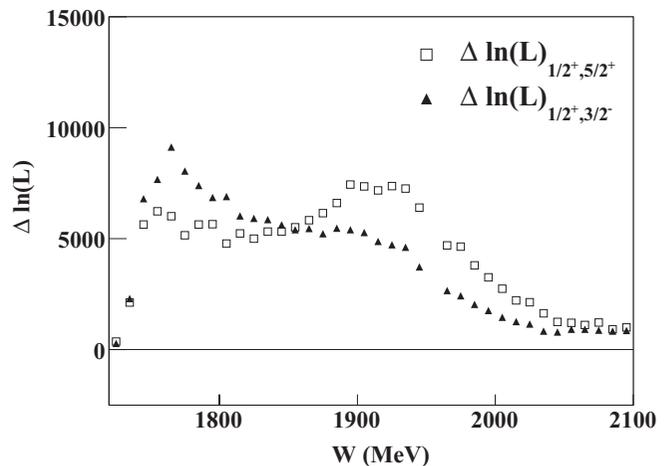


FIG. 2.  $\Delta \ln \mathcal{L}$  vs  $W$  (MeV): Example likelihood differences from  $s$ -channel scans. Each fit contained the locked OTL  $t$ -channel terms, along with a single  $s$ -channel wave. Shown are  $\Delta \ln \mathcal{L}_{1/2^+, 5/2^+} = \ln \mathcal{L}_{5/2^+} - \ln \mathcal{L}_{1/2^+}$  (open squares) and  $\Delta \ln \mathcal{L}_{1/2^+, 3/2^-} = \ln \mathcal{L}_{3/2^-} - \ln \mathcal{L}_{1/2^+}$  (closed triangles). See text for details and discussion.

Figure 2 shows two examples comparing the likelihood differences between fits with different  $s$ -channel waves. The  $\Delta \ln \mathcal{L}$  quantities are shown for two separate fits, one with  $J^P = 5/2^+$  and one with  $J^P = 3/2^-$ , each of which is compared to a fit with  $J^P = 1/2^+$ . From threshold up to  $W \sim 1.85 \text{ GeV}$ , the fit with  $J^P = 3/2^-$  is clearly the best, while in the energy range  $1.85 \text{ GeV} < W < 2 \text{ GeV}$  the preferred wave is  $J^P = 5/2^+$ . It is also clear in Fig. 2 that both the  $J^P = 3/2^-$  and  $J^P = 5/2^+$  waves provide better descriptions of our data than the  $J^P = 1/2^+$  wave in this energy range.

Similar fits were run using any single  $s$ -channel wave with  $J \leq 9/2$  of both parities. In the region from threshold up to  $W \sim 1.85 \text{ GeV}$ , the  $J^P = 3/2^-$  wave was found to provide a better description of our data than any other wave. Similarly, in the energy range  $1.85 \text{ GeV} < W < 2 \text{ GeV}$ , the  $J^P = 5/2^+$  wave was found to provide the best description.

Scans were also performed using two  $s$ -channel waves and the OTL  $t$ -channel terms. The quantity  $\Delta \ln \mathcal{L}$  can also be used in these fits to determine which wave sets best describe our data. In the  $W < 2 \text{ GeV}$  region, the best fit was obtained using the  $s$ -channel waves with  $J^P = 3/2^-, 5/2^+$ . This wave set had the best likelihood in every bin in this energy range (typically by a large amount). Given the results of the single wave  $s$ -channel scans discussed above, this is not a surprising result. Above  $2 \text{ GeV}$ , the preferred wave set consisted of the  $J^P = 5/2^+, 7/2^-$  waves, along with the  $t$ -channel terms. As in the lower energy range, this wave set had the best likelihood in every energy bin for  $W > 2 \text{ GeV}$ .

The results presented for the waves below were not affected by our choice of wave set; however, as the number of waves was increased so did the noise. For this reason, we have chosen to present the results from fits with at most three  $s$ -channel waves. See Sec. V for more discussion on fits with a larger number of waves.

### B. Fit I: The near-threshold region

Our preliminary  $s$ -channel scans showed that the best fit using two  $s$ -channel waves, along with the OTL  $t$ -channel terms, in the energy range  $1.72 \text{ GeV} < W < 2 \text{ GeV}$  is obtained using  $J^P = 3/2^-, 5/2^+$ . To extract any possible resonance contributions in these waves, event-based PWE fits were run using the locked OTL  $t$ -channel terms along with  $J^P = 3/2^-, 5/2^+$   $s$ -channel waves parametrized according to Eq. (21). In each energy bin, multiple fit iterations were run using random starting values for the parameters; the results presented below are always from the fit with the best likelihood.

#### 1. Cross sections and phase motion

The strength and phase of each  $s$ -channel wave were completely free to vary in each energy bin, i.e., they were fit independently. The cross sections extracted for the  $s$ -channel waves are consistent with either near or subthreshold resonance states (see Fig. 3). The Particle Data Group (PDG) [24] lists two states in these waves consistent with this hypothesis: (1) the four-star  $F_{15}(1680)$ , which has a well known very large coupling to  $\gamma p$ ; (2) the three-star  $D_{13}(1700)$ , which is currently rated as having only a two-star coupling to  $\gamma p$ . We note here that the masses of the states cannot be (precisely) estimated by simply examining the cross sections due to threshold suppression effects.

Figure 4 shows the phase motion between the two  $s$ -channel waves obtained from the PWE fits. The phase differences were then fit in a MDF using the constant width Breit-Wigner line shapes of the form given in Eq. (22). We chose not to use mass-dependent widths in the Breit-Wigner line shapes (despite the proximity to  $p\omega$  threshold) since the  $F_{15}(1680)$  [and perhaps the  $D_{13}(1700)$  as well] is below threshold, which introduces model dependence in a single-channel analysis. For this reason, extracting precise values for the resonance parameters may not be possible; however, the use of Eq. (22)

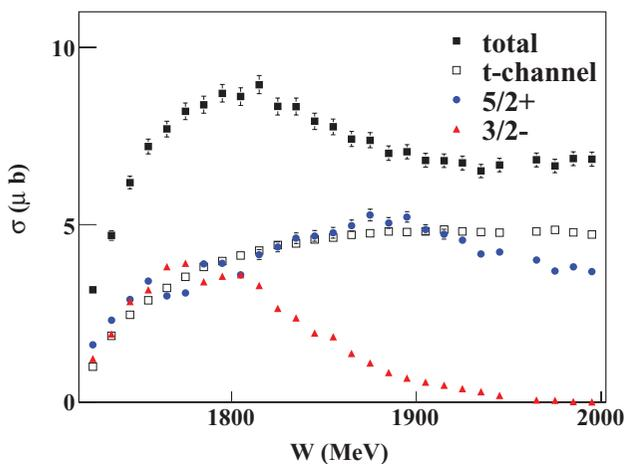


FIG. 3. (Color online) Results from Fit I:  $\sigma$  ( $\mu\text{b}$ ) vs  $W$  (MeV): Total cross sections from all of the waves included in the fit (filled squares), only  $t$ -channel waves (open squares), only  $J^P = 5/2^+$  waves (circles), and only  $J^P = 3/2^-$  waves (triangles). The cross sections extracted for both  $s$ -channel waves are consistent with near/sub-threshold resonances. The error bars are purely statistical.

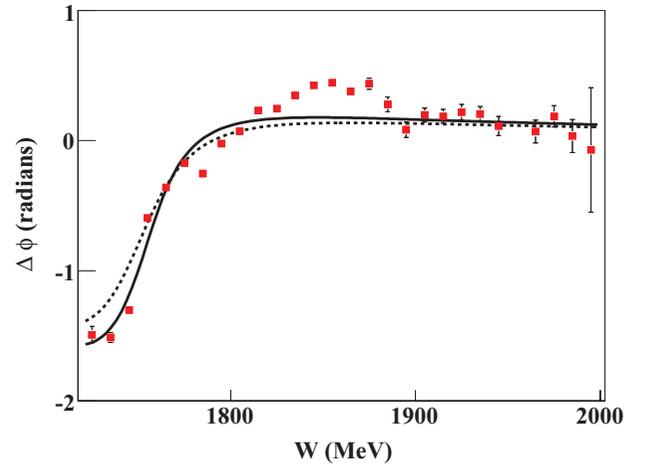


FIG. 4. (Color online) Results from Fit I:  $\Delta\phi = \phi_{3/2^-} - \phi_{5/2^+}$  (radians) vs  $W$  (MeV): The dashed line was fit using constant width Breit-Wigner distributions requiring the parameters to be within the limits quoted by the PDG for the four-star  $F_{15}(1680)$  and three-star  $D_{13}(1700)$ . The solid line was fit allowing the  $3/2^-$  parameters to vary freely, the results are listed in the text. The error bars are purely statistical.

is sufficient to provide evidence for the presence of known PDG states in our data.

In principle, our MDF fits could have been made to the partial-wave intensities as well as the phase difference. In order to do this, form factors would need to be introduced at both the production and decay vertices. While these form factors do not strongly influence the phase difference, they are very important for describing the shapes of the cross sections. The intensities of the partial waves (in this fit, and in the following sections) are qualitatively consistent with the expected resonance shapes. Obtaining good quantitative agreement requires the extra degrees of freedom introduced by the form factors; however, including these factors also introduces additional model dependence. Thus, we have decided to only fit the phase difference—which, as noted, is nearly independent of the form factors.

Our results are, qualitatively, in good agreement with those expected from the PDG states mentioned above. The dashed-line in Fig. 4 was fit requiring all parameters to be within the limits quoted by the PDG for the  $F_{15}(1680)$  and  $D_{13}(1700)$ . There is a minor discrepancy in the near-threshold bins. The parameters of the  $D_{13}(1700)$  are not as well known as those of the  $F_{15}(1680)$ ; thus, we also performed a MDF allowing the  $3/2^-$  parameters to vary freely. This fit resulted in a mass of 1754 MeV and a width of 39 MeV for the  $D_{13}(1700)$ , which are very close to the PDG limits. Uncertainties of 21 MeV for the mass and 12 MeV for the width were estimated by examining the variation in the  $3/2^-$  parameters while using various parameter values (all within the PDG limits) for the  $5/2^+$ , along with fitting different subranges in  $W$  of the phase motion.

A single channel analysis is not the best environment for extracting precise resonance parameters; however, the qualitative agreement of the phase motion obtained from the PWE's to that of the two PDG states is very suggestive of their

presence in our data. Recall that the phase parameters were each started pseudorandomly in the range  $[0, 2\pi)$  in each  $W$  bin. Yet the results are in good qualitative agreement with the phase motion expected using simple constant width Breit-Wigner distributions for the PDG  $F_{15}(1680)$  and  $D_{13}(1700)$  states.

## 2. Production helicity amplitudes

We can also compare the production helicity couplings extracted from our fits to those quoted by the PDG. The ratio of the helicity amplitudes is obtained using the production couplings,  $g_{LS}^{J^P}$  in Eq. (21), extracted by the fits and the  $s$ -channel production amplitudes. Due to the nature of the covariant formalism, these amplitudes are energy-dependent; i.e., the ratio of the helicity amplitudes is a function of  $W$ . The PDG quotes these values at the resonance masses. For the  $D_{13}(1700)$ , the PDG reports the ratio of the helicity amplitudes as [24]

$$\frac{A_{3/2}}{A_{1/2}} = 0.11 \pm 1.34. \quad (23)$$

Our fits extract this value to be in the range  $[-0.06, 0.13]$ , depending on the mass of the  $J^P = 3/2^-$  state. This is in a very good agreement with the PDG value.

The ratio of the helicity amplitudes for the  $F_{15}(1680)$  extracted by our fits is consistent with the PDG [24] value. However, projecting this ratio from the  $p\omega$  threshold down to the required mass makes obtaining a precise quantitative value difficult.

## 3. Comparison to observables

Fit I consists of three production mechanisms: (1) OTL  $t$ -channel terms (with no free parameters), which are dominated by  $\pi^0$  exchange in this energy range; (2)  $J^P = 3/2^-$   $s$ -channel waves, whose extracted parameters are consistent with the PDG  $D_{13}(1700)$  state; (3)  $J^P = 5/2^+$   $s$ -channel waves, whose extracted parameters are consistent with the PDG  $F_{15}(1680)$  state (at least, near threshold). This is almost certainly not all of the physics contributing to  $\omega$  photoproduction in this energy range. Thus, we would not expect Fit I to provide a perfect description of our data. Before we examine the quality of Fit I, we note that the OTL  $t$ -channel terms do provide a good description of our forward data in the energy regime of Fit I.

Figures 5 and 6 show comparisons of the differential cross sections and spin-density matrix elements extracted from the PWA fits compared to our measurements [11]. Recall that we do not fit to the experimental observables directly. We perform event-based fits to the data used to obtain the measured results. The forward cross section and polarization observables are very well described in this energy range, confirming that  $\pi^0$  exchange in the  $t$  channel does dominate the amplitude in this region. There is a discrepancy in the description of the cross section at backward angles that increases with energy. This could be due to the lack of  $u$ -channel terms. It could also be a signature of unaccounted-for  $s$ -channel amplitudes.

Though we did not start off by including known PDG resonance states, the fit has extracted evidence for them

from our data. We also note here that the large-angle cross section at  $W = 1.8$  GeV is virtually flat. Without polarization information, the production mechanism could have easily been mistaken for a  $J = 1/2$  wave. This demonstrates the importance of the spin-density matrix elements.

The quality of the description of the observables decreases slightly with increasing energy. This signifies that there is another production mechanism that is not accounted for in the fit. This is expected due to the limited number of waves included in the PWA. Adding additional waves improves the description of the data but has virtually no effect on the strengths and phase motion of the two  $s$ -channel waves presented in this section. Thus, the conclusions drawn about resonance contributions are robust, and do not change when additions are made to the wave set. See Sec. IV D1 for results obtained by adding an additional  $s$ -channel wave to this fit.

## C. Fit II: The higher mass region

Our preliminary  $s$ -channel scans showed that the best fit using two  $s$ -channel waves and the OTL  $t$ -channel terms in the energy range  $2 \text{ GeV} < W < 2.4 \text{ GeV}$  is obtained using waves with  $J^P = 5/2^+, 7/2^-$ . To extract any possible resonance contributions in these waves, the same procedure used for Fit I was employed.

### 1. Cross sections and phase motion

As in Fit I, the strength and phase of each  $s$ -channel wave were completely free to vary in each energy bin in the PWE's. The cross sections extracted for the  $s$ -channel waves, shown in Fig. 7, are consistent with the tail of a  $J^P = 5/2^+$  state with a mass below 2 GeV (as seen in Fit I) and a  $J^P = 7/2^-$  state with a mass near 2.2 GeV. The PDG lists a state consistent with this hypothesis: the four-star  $G_{17}(2190)$ , which currently is only listed as having one-star coupling to  $\gamma p$ .

Figure 8 shows the phase motion between the two  $s$ -channel waves extracted from the PWE's. Our results do not agree with those expected from the PDG  $F_{15}(1680)$  and  $G_{17}(2190)$  states, assuming their mass dependencies are well described by the constant width Breit-Wigner line shape described in Eq. (22). Allowing the  $J^P = 5/2^+$  parameters to vary freely gives us better agreement and yields a mass around 1.95 GeV. The presence of a second state in the  $J^P = 5/2^+$  wave near this mass would have virtually no effect on the results obtained in Fit I; however, it would mean that the use of a Breit-Wigner distribution in the energy range where both  $5/2^+$  states are contributing significantly, e.g., the energy region examined in Fit II, is invalid.

Instead, we can employ a two-pole single channel  $K$ -matrix for the  $5/2^+$  states of the form [25]

$$K(s) = \sum_{\alpha=1}^2 \frac{g_{\alpha p\omega}^2 B_\ell^2(s)}{w_\alpha^2 - s}, \quad (24)$$

where  $w_\alpha$  and  $g_{\alpha p\omega}$  are the  $K$ -matrix resonance masses and coupling constants to the  $p\omega$  final state and  $B_\ell$  are the centrifugal barrier factors (see, e.g., [23]). The mass dependence of the amplitude is then written in terms of the

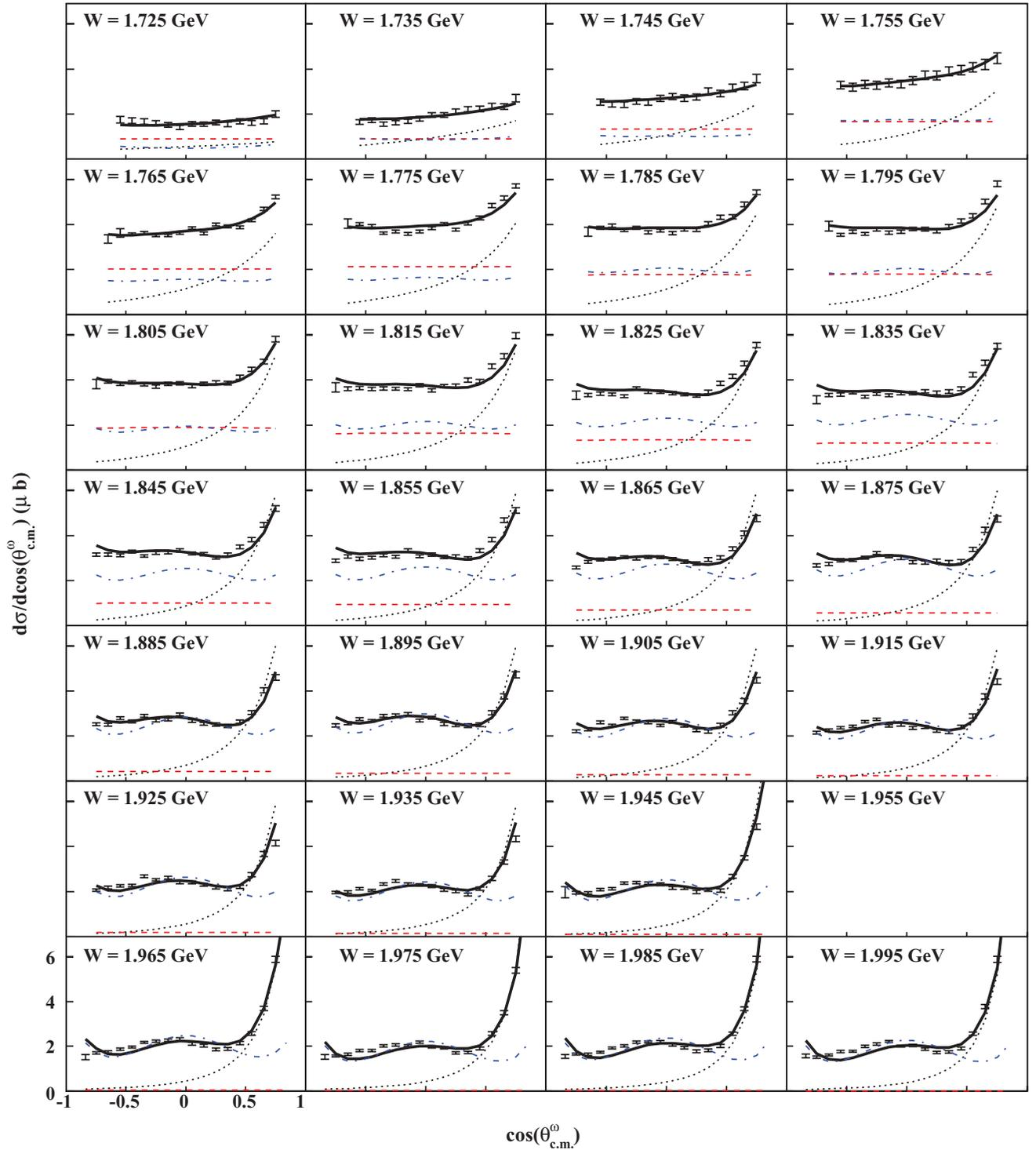


FIG. 5. (Color online)  $d\sigma/d\cos\theta_{c.m.}^{\omega}$  ( $\mu\text{b}$ ) vs  $\cos\theta_{c.m.}^{\omega}$ : PWA results from Fit I (solid black line), compared to our measurements [11]. The individual contributions from the  $J^P = 3/2^-$  wave (red, dashed line),  $J^P = 5/2^+$  wave (blue, dashed-dotted line), and OTL  $t$ -channel terms (dotted black line) are also shown. The lack of data reported in the  $W = 1.955$  GeV bin is due to normalization issues [11].

production vector,  $P$ , and two-body phase-space factor, where  $\rho$ , as

$$\mathcal{R}_{5/2^+}(s) = P(1 - i\rho K)^{-1}, \quad (25)$$

$$P = \sum_{\alpha=1}^2 \frac{g_{\alpha\gamma\gamma} g_{\alpha\rho\omega} B_{\ell}(s)}{w_{\alpha}^2 - s}, \quad (26)$$

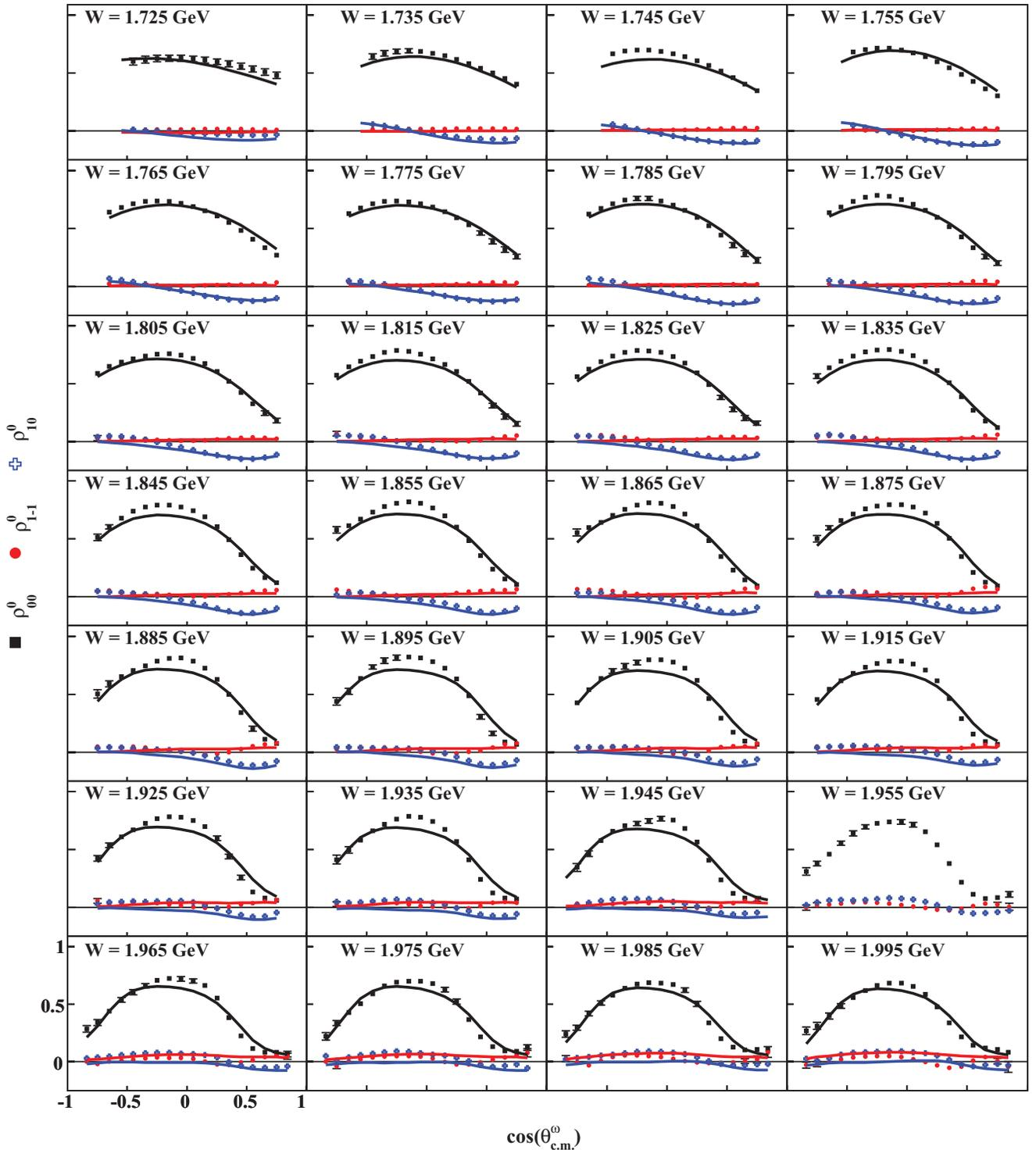


FIG. 6. (Color online)  $\rho_{MM'}^0$  vs  $\cos\theta_{c.m.}^0$ : PWA results from Fit I:  $\rho_{00}^0$  (solid black line),  $\rho_{1-1}^0$  [solid middle (red) line],  $\text{Re}\rho_{10}^0$  [solid bottom (blue) line], compared to our measurements [11]. The lack of a fit in the  $W = 1.955$  GeV bin is due to normalization issues [11].

with production coupling constants  $g_{\alpha p \gamma}$  and

$$\rho = \frac{\sqrt{[s - (w_\omega + w_p)^2][s - (w_\omega - w_p)^2]}}{s}. \quad (27)$$

For this MDF, we required the  $J^P = 7/2^-$  parameters to be within the limits quoted by the PDG for the  $G_{17}(2190)$ . One of

the  $J^P = 5/2^+$   $K$ -matrix poles was required to be consistent with the  $F_{15}(1680)$ . The exact location of this pole depends on how one treats the opening of the  $p\omega$  threshold (this is a single channel analysis). The parameters of the second  $J^P = 5/2^+$   $K$ -matrix pole were obtained from the MDF yielding 1930 MeV for the mass and 100 MeV for the width. Even with

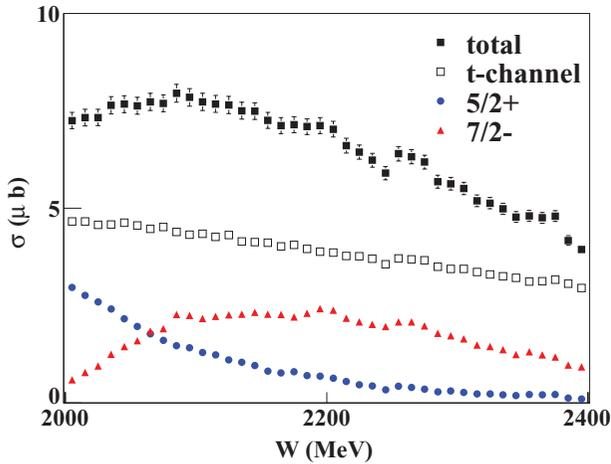


FIG. 7. (Color online) Results from Fit II:  $\sigma$  ( $\mu\text{b}$ ) vs  $W$  (MeV): Total cross sections from all of the waves in the fit (filled squares), only  $t$ -channel waves (open squares), only  $J^P = 5/2^+$  waves (circles), and only  $J^P = 7/2^-$  waves (triangles). The cross section extracted for  $J^P = 5/2^+$  is consistent with the tail of a lower mass state (as seen in Fit I). The  $J^P = 7/2^-$  cross section is indicative of a state near 2.2 GeV. The errors are purely statistical.

these constraints, the results provide a very good description of the phase motion obtained from the PWE.

In principle, poles in the  $T$ -matrix and poles in the  $K$ -matrix can be quite different. The relationship between the two can also depend on the specific  $K$ -matrix model employed. For these reasons, care must be taken when interpreting the parameters obtained for the “second”  $5/2^+$  resonance. While the  $K$ -matrix parameters may not coincide exactly with the

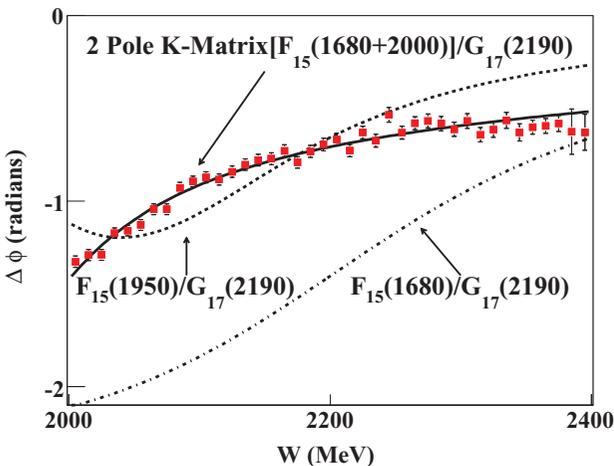


FIG. 8. (Color online) Results from Fit II:  $\Delta\phi = \phi_{7/2^-} - \phi_{5/2^+}$  (radians) vs  $W$  (MeV): The dot-dashed line is the phase motion expected using constant width Breit-Wigner distributions and the parameters quoted by the PDG for the  $F_{15}(1680)$  and  $G_{17}(2190)$ . The dashed line required the  $J^P = 7/2^-$  parameters to be within the PDG limits for the  $G_{17}(2190)$ , while allowing the  $J^P = 5/2^+$  parameters to vary freely. The solid line used a constant width Breit-Wigner distribution for the  $G_{17}(2190)$ , but a two-pole single channel  $K$ -matrix for the  $J^P = 5/2^+$  wave. The parameters obtained from these fits are listed in the text. The error bars are purely statistical.

physical  $T$ -matrix values, the observed strength in this wave and its phase motion relative to the  $G_{17}(2190)$  support it having a mass around 1.9–2 GeV and a width of approximately 200–300 MeV. These values are in good agreement with the missing  $F_{15}(2000)$  state predicted by [26]. A check using the (unitarity violating) two Breit-Wigner prescription also resulted in  $5/2^+$  resonance parameters in this range. To extract precise resonance parameters for this state (and to confirm its existence), a coupled-channel analysis should be employed.

## 2. Production helicity amplitudes

The ratio of the helicity amplitudes for the  $F_{15}(1680)$  was discussed in Sec. IV B2. Without employing a model we cannot separate out the possible missing  $F_{15}(2000)$  production amplitudes. The ratio of the helicity amplitudes for the  $G_{17}(2190)$  is extracted to be

$$\frac{A_{3/2}}{A_{1/2}} = -0.17 \pm 0.15. \quad (28)$$

Due to its one-star coupling to  $\gamma p$ , the PDG does not quote a value for this ratio.

## 3. Comparison to observables

As in Fit I, we do not expect the limited number of waves used in Fit II to include all of the physics at these energies. Thus, we again do not expect to provide a perfect description of the observables in this energy regime. Before we examine Fit II, we note that the OTL  $t$ -channel terms provide a good description of our forward cross sections; however, there are some noticeable discrepancies with the spin-density matrix elements at these energies [22].

Figures 9 and 10 show the differential cross sections and spin-density matrix elements extracted from the PWA fits compared to our measurements [11]. As the energy increases, the quality of the descriptions of the spin-density matrix elements decreases. This is partly due to the issues with the nonresonant model employed (as discussed in Sec. III B). At these energies, the OTL  $t$ -channel terms begin to fail to adequately describe the polarization observables. The discrepancies in the backward direction could be due to the lack of inclusion of any  $u$ -channel terms. The effects on our results, i.e., the effects on conclusions drawn about resonance contributions, due to possible issues with the nonresonant terms are discussed in Sec. V.

The lack of perfect description of the data signifies that there are other production mechanisms that are not accounted for in the fit. This is, again, expected due to the limited number of waves included in the PWA. Adding additional waves improves the description of the data. The strengths and phase motion of the two  $s$ -channel waves presented in this section become noisier in the presence of these additional waves; however, the conclusions drawn about resonance contributions are unaffected by additions to the wave set. We are unable to determine from our PWE’s which additional waves may coincide with unaccounted-for physical processes; thus, we do not present them here. Perhaps future measurement of additional polarization observables in this energy range might help determine the nature of these waves.

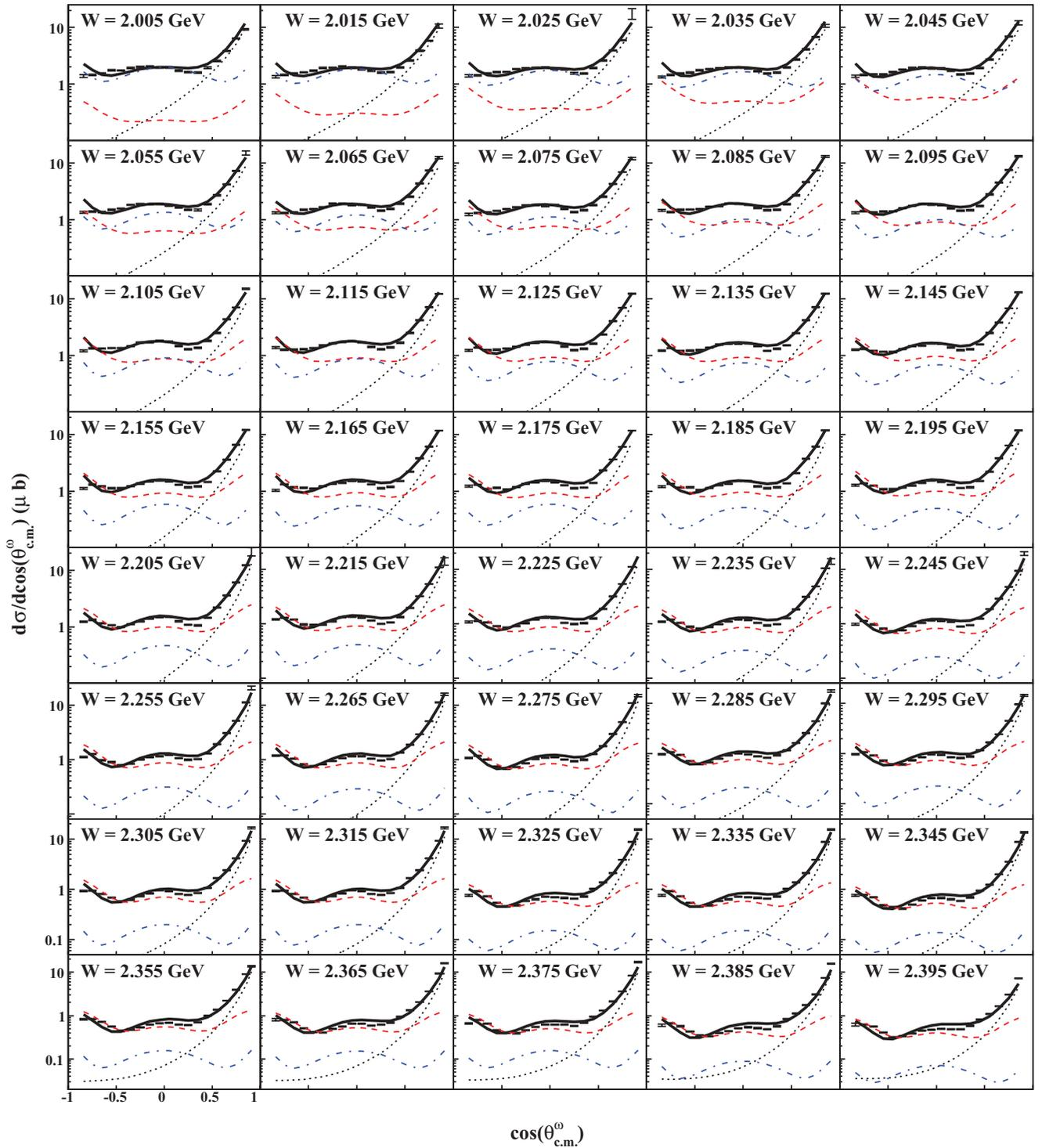


FIG. 9. (Color online)  $d\sigma/d\cos\theta_{\text{c.m.}}^{\omega}$  ( $\mu\text{b}$ ) vs  $\cos\theta_{\text{c.m.}}^{\omega}$ : PWA results from Fit II (solid black line), compared to our measurements [11]. The individual contributions from the  $J^P = 7/2^-$  wave (red, dashed line),  $J^P = 5/2^+$  wave (blue, dashed-dotted line), and OTL  $t$ -channel terms (dotted black line) are also shown.

#### D. Evidence for additional resonance states

One of the prime motivating factors in undertaking this study was to search for missing resonances. The strongest evidence for resonance contributions to  $\omega$  photoproduction found in Fits I and II was for well-known PDG states. Suggestive evidence was also found for a missing  $F_{15}(2000)$

state. Below we examine possible additional resonance contributions.

##### 1. Fit III: The $3/2^+$ wave

Quark model calculations predict three missing resonances with  $J^P = 3/2^+$  in the energy range of Fit I which couple

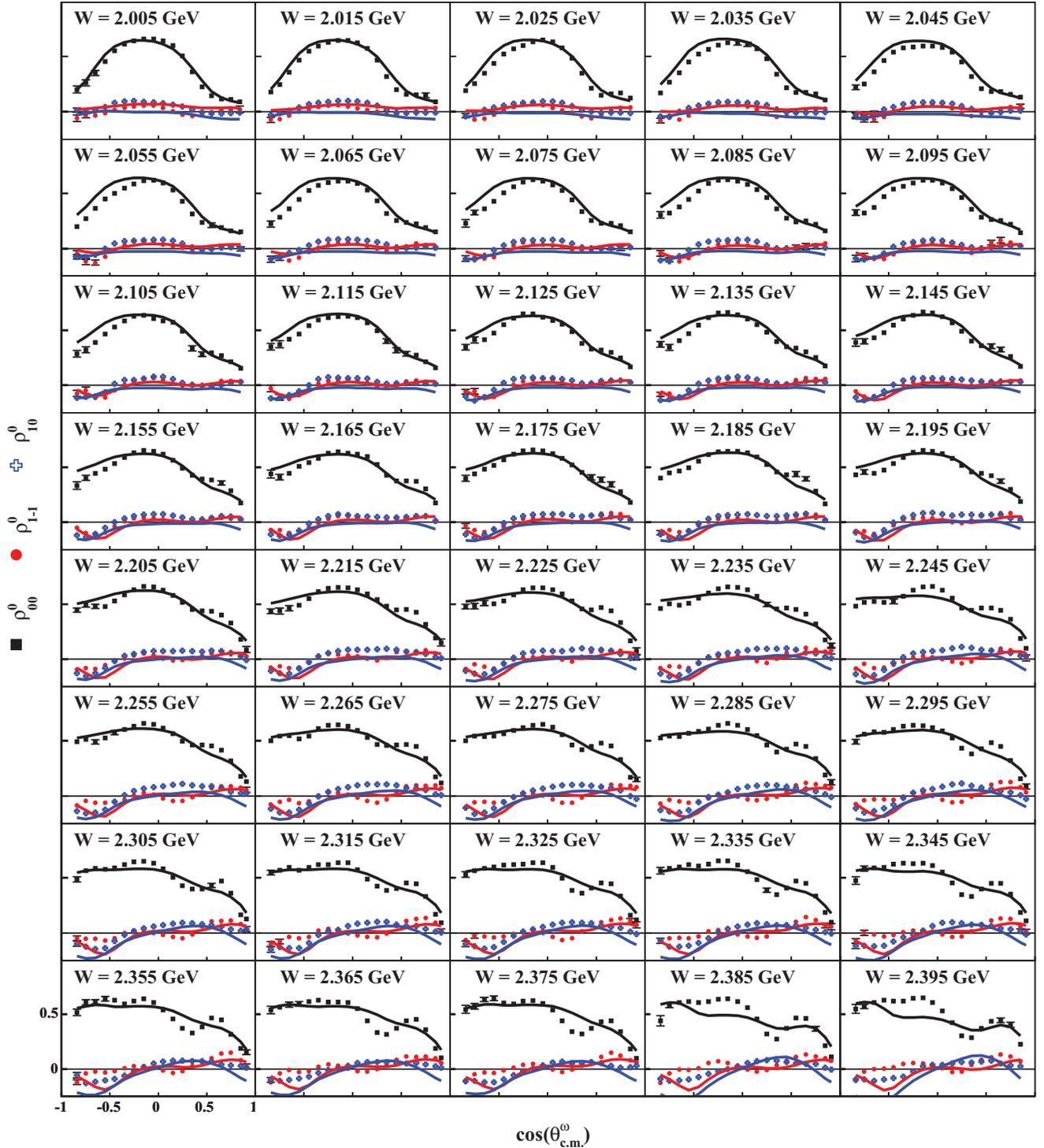


FIG. 10. (Color online)  $\rho_{MM'}^0$  vs  $\cos \theta_{c.m.}^0$ : PWA results from Fit II:  $\rho_{00}^0$  [solid upper (at the right-hand edge) line (black)],  $\rho_{1-1}^0$  [solid middle (at the right-hand edge) line (red)],  $\text{Re} \rho_{10}^0$  [solid lower (at the right-hand edge) line (blue)], compared to measurements [11]. See text for discussion.

to  $p\omega$  [26]. Figure 11 shows the cross sections and phase motion obtained if we add a  $J^P = 3/2^+$  wave to the PWE in Fit I. Below 1800 MeV, the range of production angles over which the CLAS has acceptance is limited. This makes it difficult to cleanly separate contributions from three waves; thus, this energy range has been excluded from these fits.

The strengths and phases of the  $J^P = 3/2^-, 5/2^+$  waves are virtually unaltered by the addition of the extra  $s$ -channel wave. The cross section of the  $J^P = 3/2^+$  wave does show some fairly smooth structure; however, its phase motion, relative to the other two resonant states, is not consistent with a single constant width Breit-Wigner hypothesis. If we instead perform

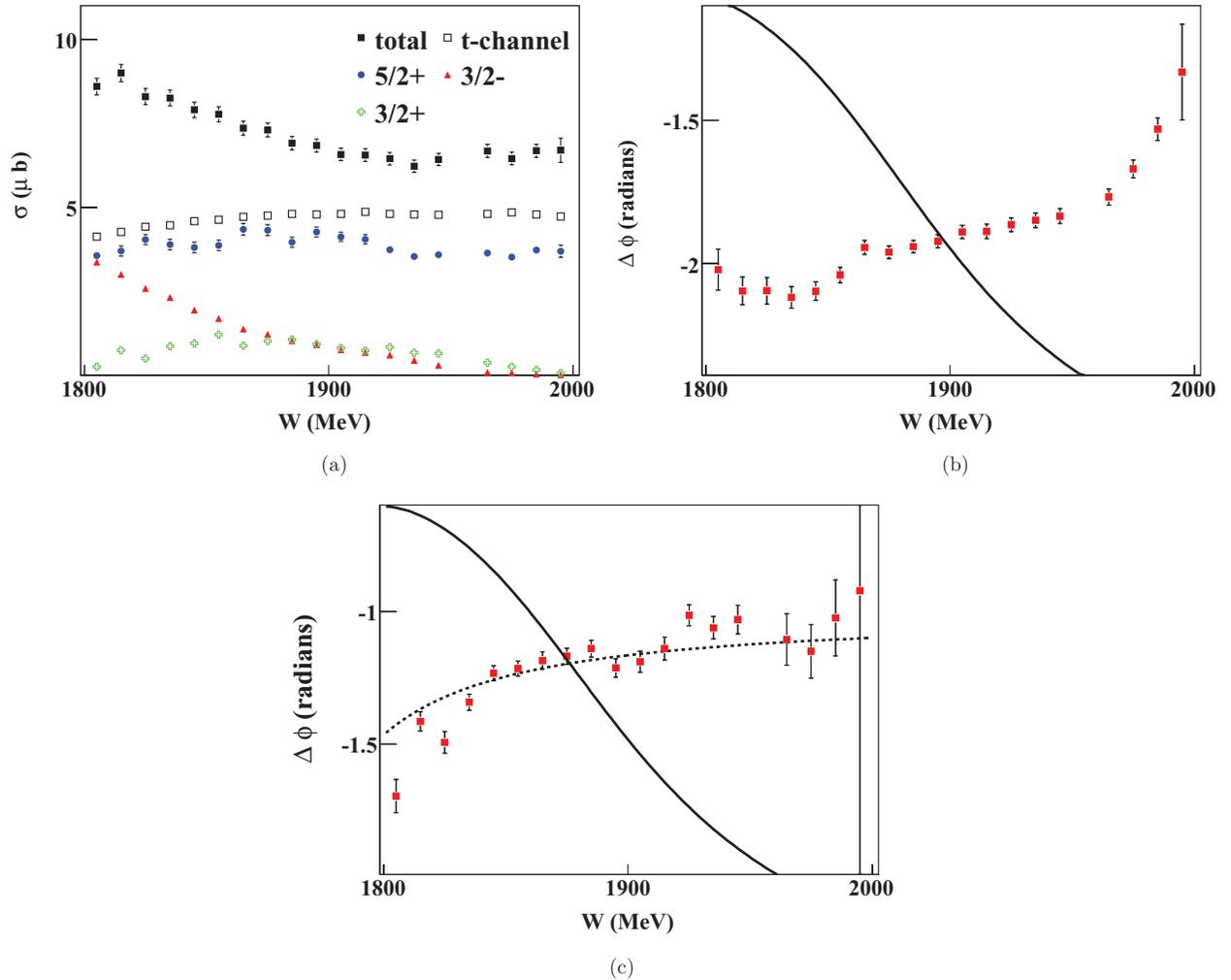


FIG. 11. (Color online) Results from Fit III: (a)  $\sigma$  ( $\mu\text{b}$ ) vs  $W$  (MeV): Total cross sections extracted from all of the waves in the fit (filled black squares), only  $t$ -channel waves (open squares), only  $5/2^+$  waves (circles), only  $3/2^-$  waves (triangles), and only  $3/2^+$  waves (crosses). (b)  $\Delta\phi = \phi_{5/2^+} - \phi_{3/2^+}$  (radians) vs  $W$  (MeV). (c)  $\Delta\phi = \phi_{3/2^-} - \phi_{3/2^+}$  (radians) vs  $W$  (MeV). The solid curves show the phase motion expected assuming the  $J^P = 3/2^+$  has Breit-Wigner parameters  $M_{3/2^+} = 1875$  MeV and  $\Gamma_{3/2^+} = 150$  MeV while locking the  $J^P = 3/2^-$  and  $J^P = 5/2^+$  parameters to be those of the  $D_{13}(1700)$  and  $F_{15}(1680)$ , respectively. The phase motion obtained for the  $3/2^+$  is not consistent with a single resonant state. The dashed line on (c) represents using the  $D_{13}(1700)$  Breit-Wigner parameters for the  $3/2^-$  and a single channel two-pole  $K$ -matrix for the  $3/2^+$ . There is enough freedom to describe the data (see text for discussion). All error bars are purely statistical.

a MDF using the  $K$ -matrix formalism described in Sec. IV C 1 for the  $J^P = 3/2^+$  wave, the phase motion between the  $J^P = 3/2^-$ ,  $3/2^+$  waves is well described. The poles in the  $K$ -matrix are at 1850 MeV and 1950 MeV. We could apply the same procedure for the  $J^P = 5/2^+$ ,  $3/2^+$  phase motion; however, both waves would have  $K$ -matrices and the number of free parameters would leave the fit underconstrained.

Figures 12 and 13 show the comparisons of the PWA results with our measurements [11]. The additional  $3/2^+$  wave improves the description of the spin-density matrix elements obtained in Fit I (see Fig. 6). It is difficult to make firm conclusions about the  $J^P = 3/2^+$  wave. The observed strength suggests there is significant overlap of the scattering amplitude with this partial wave; however, this is not sufficient evidence to claim resonance contributions. The phase motion of the  $3/2^+$  wave relative to the  $3/2^-$  and  $5/2^+$  waves is not

consistent with a single resonant state. This does not, however, rule out the existence of the multiple states predicted by the quark model.

## 2. Limitations of the mass-independent technique

Numerous other fits that we have performed yielded inconclusive evidence for states of various spin-parities. These fits are very similar to Fit III. Generally, smooth structures are found in the extracted cross sections; however, the phase motion is inconsistent with a single resonant state. It is possible that a number of resonant states exist which couple relatively strongly to  $p\omega$ . It is also possible that the smooth cross sections are simply the result of overlap of various partial waves with unaccounted-for nonresonant terms. It would appear that we

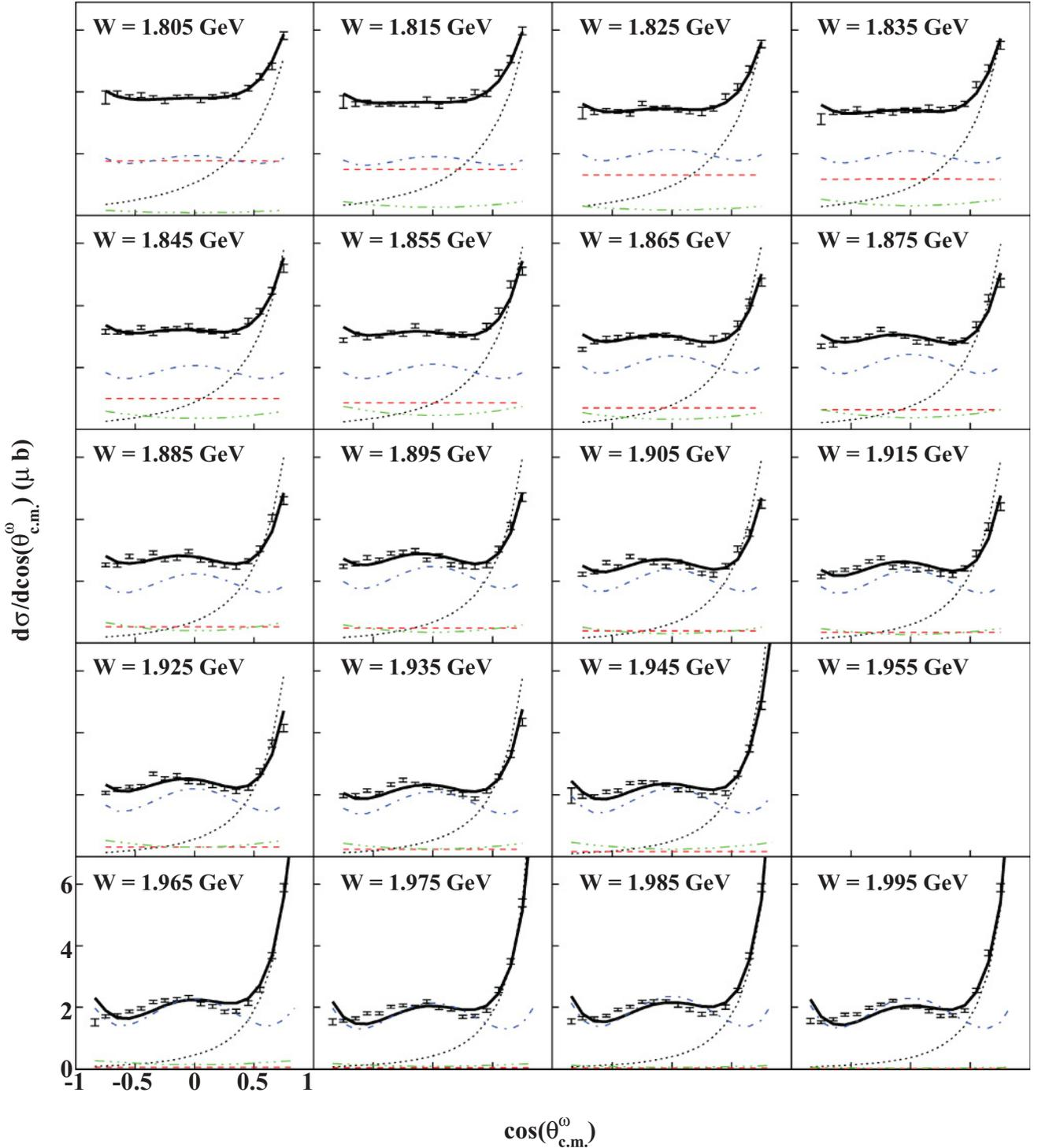


FIG. 12. (Color online)  $d\sigma/d\cos\theta_{c.m.}^{\omega}$  ( $\mu\text{b}$ ) vs  $\cos\theta_{c.m.}^{\omega}$ : PWA results from Fit III (solid black line), compared to our measurements [11]. The individual contributions from the  $J^P = 3/2^-$  wave (red, dashed line),  $J^P = 5/2^+$  wave (blue, dashed-dotted line), the  $J^P = 3/2^+$  wave (green, dashed-triple-dotted line), and OTL  $t$ -channel terms (dotted black line) are also shown. The lack of data reported in the  $W = 1.955$  GeV bin is due to normalization issues [11].

have reached the limits of what our technique can extract from our data.

More polarization information may be required to cleanly extract additional resonances. Improved theoretical input for the nonresonant (non  $s$ -channel) terms may also be necessary.

While our studies have shown that the strong  $s$ -channel signals extracted by this analysis are not affected by the way that the nonresonant terms are modeled (see Sec. V), this is almost certainly not the case for weaker signals. This is particularly true at higher energies, where the current theoretical models do

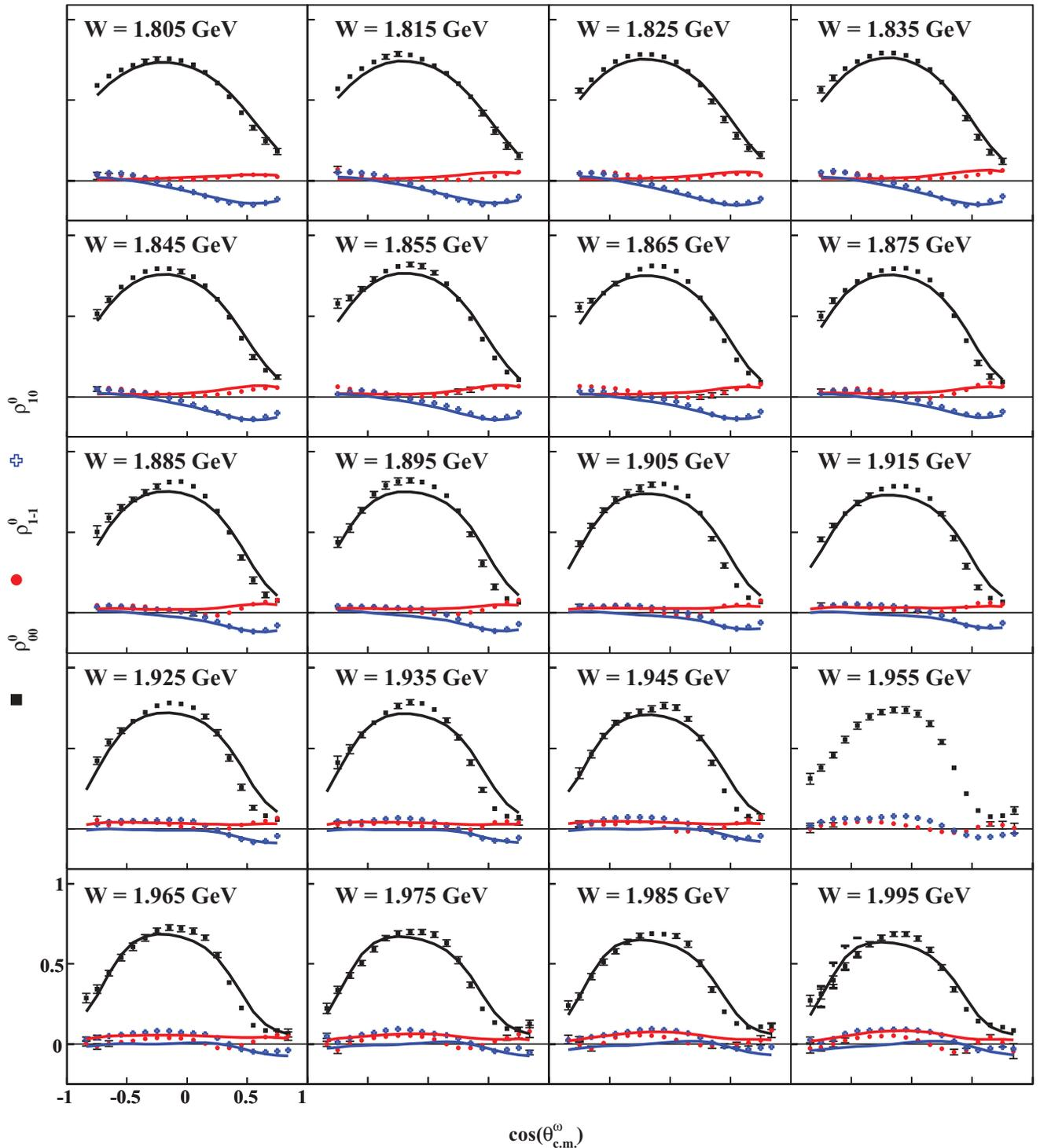


FIG. 13. (Color online)  $\rho_{MM'}^0$  vs  $\cos\theta_{c.m.}^0$ : PWA results from Fit III:  $\rho_{00}^0$  [solid upper (at the right-hand edge) line (black)],  $\rho_{1-1}^0$  [solid middle (at the right-hand edge) line (red)],  $\text{Re}\rho_{10}^0$  [solid lower (at the right-hand edge) line (blue)], compared to measurements [11]. See text for discussion.

a poor job of describing the new CLAS data. The amplitudes that are currently being generated by several groups from a coupled-channel approach (see, e.g., [27]) may well allow for the extraction of much weaker resonance signals from these data.

## V. SYSTEMATIC STUDIES

### A. *s*-channel scans

In Sec. IV A, we found that the single *s*-channel waves with the best likelihoods were  $J^P = 3/2^-$  for  $W < 1.85$  GeV and

$J^P = 5/2^+$  for  $1.85 \text{ GeV} < W < 2 \text{ GeV}$ . We proceeded to add single  $s$ -channel waves to these fits to determine which had the best likelihoods; these were the basis for the wave sets used in Fits I and II. We can also examine the “discarded” wave sets and examine the  $s$ -channel contributions as a systematic check on our results.

In the  $W < 2 \text{ GeV}$  energy range, the  $s$ -channel waves with  $J^P = 3/2^-, 5/2^+$ , used in Fit I, had the best likelihood of all two  $s$ -channel wave combinations (when combined with the OTL  $t$ -channel waves). In this fit, the contributions extracted for the two  $s$ -channel waves were approximately equal in size for  $W < 1.85 \text{ GeV}$ . For all other  $[3/2^-, J^P]$  combinations, the extracted contribution for the  $J^P = 3/2^-$  wave was the bigger of the two  $s$ -channel terms in this energy range. In the  $1.85 \text{ GeV} < W < 2 \text{ GeV}$  energy range, the  $5/2^+$  wave had the larger of the two  $s$ -channel contributions for every  $J^P$  used for the other  $s$ -channel wave. Fits were also run using all two  $s$ -channel wave combinations (with the OTL  $t$ -channel terms) over the entire energy range. The contributions of the waves presented in this paper were consistent, regardless of which other waves they were fit with.

The robustness of the results presented in this paper was also tested by performing the PWE's with larger wave sets. The presence of any additional  $J \leq 5/2$  wave does not effect the conclusions drawn about resonance contributions to Fit I or Fit II. Fits run with very large wave sets that included all  $s$ -channel waves with  $J \leq 9/2$  also confirm the large contributions from the  $J^P = 3/2^-$  and  $5/2^+$  below  $2 \text{ GeV}$  and from  $J \geq 7/2$  waves around  $2.2 \text{ GeV}$ ; however, with this many waves it was not possible to unambiguously determine the spin-parity of the large  $J$  contribution.

### B. Including $u$ -channel terms

Another possible cause of systematic effects is our lack of inclusion of any  $u$ -channel terms. For  $W < 2 \text{ GeV}$ , any  $u$ -channel contribution must be small due to the lack of any visible peak in the backward cross section. Thus, the conclusions drawn from Fit I are independent of whether or not  $u$ -channel terms are included. The same cannot be said for the energy regime of Fit II. In [22], we were able to modify the  $u$ -channel parameters of the Oh, Titov, and Lee model to better describe our highest energy data; however, these amplitudes were not included in our PWA fits due to a lack of confidence in the assumptions used to obtain the parameters.

We can examine what effect adding these terms would have on the resonance parameters extracted in Fit II. Figure 14 shows the phase motion obtained from Fit II with and without  $u$ -channel amplitudes. The agreement is very good in the region where both of the  $s$ -channel waves have strong contributions to the cross section. It is only in the regions where the cross section of one of the  $s$ -channel terms is very small that including  $u$ -channel terms leads to a discrepancy in the extracted phase motion. Therefore, the conclusions drawn from Fit II regarding the resonance states are unaffected by how the  $u$ -channel terms are modeled.

We also note here that the likelihoods of the fits containing the  $u$ -channel terms were worse in all bins. Perhaps this is not surprising since the modified OTL terms were obtained

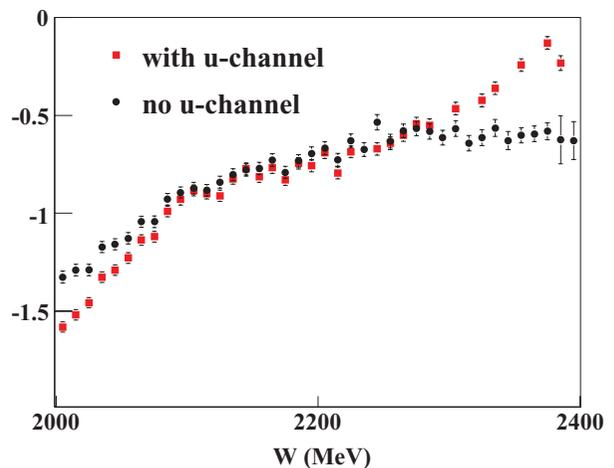


FIG. 14. (Color online) Fit II + $u$ -channel:  $\Delta\phi = \phi_{7/2^-} - \phi_{5/2^+}$  (radians) vs  $W$  (MeV): Phase motion obtained with and without  $u$ -channel terms in Fit II. Including  $u$ -channel terms only creates discrepancies in the phase motion where one of the  $s$ -channel waves has a small contribution to the cross section. The error bars on both phase motion plots are purely statistical.

assuming the entire backward production amplitude is due to  $u$ -channel mechanisms at our highest energies. To obtain a better  $u$ -channel model, the OTL parameters should be fit including  $s$ -channel waves; however, to simply estimate the effects of neglecting  $u$ -channel terms in Fit II, these parameters are sufficient.

## VI. CONCLUSIONS

An event-based mass-independent partial wave analysis has been performed on data obtained using the CLAS at Jefferson Lab. Evidence has been found for contributions from the  $F_{15}(1680)$  and  $D_{13}(1700)$  nucleon resonance states. These states are found to be dominant near threshold. The data also strongly support the presence of the  $G_{17}(2190)$  state. Suggestive evidence for an additional  $5/2^+$  state with a mass around  $1.9\text{--}2 \text{ GeV}$  has also been found. The data shows definite strength in this partial wave over a very large energy range. The phase motion between this wave and the  $G_{17}(2190)$  supports the presence of a second  $5/2^+$  state near  $1.95 \text{ GeV}$ . Some evidence for other states exists, although the interpretations are more difficult. The strength seen in the  $J^P = 3/2^+$  wave around  $W = 1.8\text{--}2 \text{ GeV}$ , for example, is not consistent with a single resonant state; however, we cannot rule out the possibility that multiple  $3/2^+$  resonances could be contributing to our data at these energies. To extract additional resonance signals from our data, improved theoretical input for the nonresonant terms may be required. In particular, including the amplitudes currently being generated by coupled-channel analyses would be highly desirable.

## ACKNOWLEDGMENTS

We thank the staff of the Accelerator and the Physics Divisions at Thomas Jefferson National Accelerator Facility who made this experiment possible. This work was supported

in part by the US Department of Energy (under Grant No. DE-FG02-87ER40315), the National Science Foundation, the Italian Istituto Nazionale di Fisica Nucleare, the French Centre National de la Recherche Scientifique, the French Commissariat à l’Energie Atomique, the Science and Tech-

nology Facilities Council (STFC), and the Korean Science and Engineering Foundation. The Southeastern Universities Research Association (SURA) operated Jefferson Lab under US DOE Contract No. DE-AC05-84ER40150 during this work.

- 
- [1] J. Ballam *et al.*, Phys. Rev. D **7**, 3150 (1973).  
 [2] R. W. Clift *et al.*, Phys. Lett. **B72**, 144 (1977).  
 [3] D. P. Barber *et al.* (LAMP2 Group Collaboration), Z. Phys. C **26**, 343 (1984).  
 [4] M. Battaglieri *et al.* (CLAS Collaboration), Phys. Rev. Lett. **90**, 022002 (2003).  
 [5] J. Barth *et al.* (SAPHIR Collaboration), Eur. Phys. J. A **18**, 117 (2003).  
 [6] Y. Oh, A. I. Titov, and T. S. H. Lee, Phys. Rev. C **63**, 025201 (2001).  
 [7] A. I. Titov and T. S. H. Lee, Phys. Rev. C **66**, 015204 (2002).  
 [8] Q. Zhao, Phys. Rev. C **63**, 025203 (2001).  
 [9] G. Penner and U. Mosel, Phys. Rev. C **66**, 055212 (2002).  
 [10] V. Shklyar, H. Lenske, U. Mosel, and G. Penner, Phys. Rev. C **71**, 055206 (2005).  
 [11] M. Williams *et al.* (CLAS Collaboration), Phys. Rev. C **80**, 065208 (2009).  
 [12] K. Schilling, P. Seyboth, and G. Wolf, Nucl. Phys. **B15**, 397 (1970).  
 [13] D. I. Sober *et al.*, Nucl. Instrum. Methods Phys. Res. A **440**, 263 (2000).  
 [14] M. Williams, Ph.D. thesis, Carnegie Mellon University, 2007, [www.jlab.org/Hall-B/general/clas\\_thesis.html](http://www.jlab.org/Hall-B/general/clas_thesis.html).  
 [15] B. A. Mecking *et al.*, Nucl. Instrum. Methods Phys. Res. A **503**, 513 (2003).  
 [16] S. U. Chung, BNL preprint BNL-QGS-93-05 (1999).  
 [17] M. Williams, M. Bellis, and C. A. Meyer, JINST **4**, P10003 (2009).  
 [18] M. Williams, Comput. Phys. Commun. **180**, 1847 (2009).  
 [19] D. Binosi and L. Theussl, Comput. Phys. Commun. **161**, 76 (2004).  
 [20] C. Zemach, Phys. Rev. **140**, B109 (1965).  
 [21] A. Donnachie and P. V. Landshoff, Phys. Lett. **B296**, 227 (1992).  
 [22] M. Williams *et al.*, “The impact on the phenomenology of  $\gamma p \rightarrow p\omega$  of the first high-precision measurements of  $\omega$  polarization observables,” Phys. Rev. (to be submitted).  
 [23] A. V. Anisovich *et al.*, Eur. Phys. J. A **24**, 111 (2005).  
 [24] C. Amsler *et al.* (Particle Data Group), Phys. Lett. **B667**, 1 (2008).  
 [25] C. Amsler *et al.* (Crystal Barrel Collaboration), Phys. Lett. **B355**, 425 (1995).  
 [26] S. Capstick and W. Roberts, Phys. Rev. D **49**, 4570 (1994).  
 [27] M. W. Paris, Phys. Rev. C **79**, 025208 (2009).